J Sci Comput (2009) 40: 51–85
DOI 10.1007/s10915-008-9266-9

Nonconforming Maxwell Eigensolvers

Susanne C. Brenner · Fengyan Li · Li-yeng Sung

Received: 23 May 2008 / Revised: 5 December 2008 / Accepted: 17 December 2008 /
Published online: 22 January 2009

Abstract Three Maxwell eigensolvers are discussed in this paper. Two of them use classical nonconforming finite element approximations, and the other is an interior penalty type discontinuous Galerkin method. A main feature of these solvers is that they are based on the formulation of the Maxwell eigenproblem on the space $H_0(\mathrm{curl};\Omega)\cap H(\mathrm{div}^0;\Omega)$. These solvers are free of spurious eigenmodes and they do not require choosing penalty parameters. Furthermore, they satisfy optimal order error estimates on properly graded meshes, and their analysis is greatly simplified by the underlying compact embedding of $H_0(\mathrm{curl};\Omega)\cap H(\mathrm{div}^0;\Omega)$ in $L_2(\Omega)$. The performance and the relative merits of these eigensolvers are demonstrated through numerical experiments.

Keywords Maxwell eigenvalues · Nonconforming finite element method · Interior penalty method · Spurious eigenvalues

The work of S.C. Brenner was supported in part by the National Science Foundation under Grant No. DMS-07-38028, and Grant No. DMS-07-13835.
The work of F. Li was supported in part by the National Science Foundation under Grant No. DMS-06-52481, and by the Alfred P. Sloan Foundation as an Alfred P. Sloan Research Fellow.
The work of L. Sung was supported in part by the National Science Foundation under Grant No. DMS-07-13835.

S.C. Brenner
Department of Mathematics and Center for Computation and Technology, Louisiana State University, Baton Rouge, LA 70803, USA
e-mail: brenner@math.lsu.edu

F. Li (✉)
Department of Mathematical Sciences, Rensselaer Polytechnic Institute, Troy, NY 12180, USA
e-mail: lif@rpi.edu

L. Sung
Department of Mathematics, Louisiana State University, Baton Rouge, LA 70803, USA
e-mail: sung@math.lsu.edu

1 Introduction

The computation of Maxwell eigenvalues is of fundamental importance in computational electromagnetism. In this paper, we consider the following Maxwell eigenproblem with the perfectly conducting boundary condition:

Find $(\mathring{\boldsymbol{u}}, \lambda) \in H_0(\mathrm{curl};\Omega) \cap H(\mathrm{div}^0;\Omega) \times \mathbb{R}$ such that $\mathring{\boldsymbol{u}} \neq \mathbf{0}$ and

$$(\nabla \times \mathring{\boldsymbol{u}}, \nabla \times \boldsymbol{v}) = \lambda(\mathring{\boldsymbol{u}}, \boldsymbol{v}) \quad \forall \boldsymbol{v} \in H_0(\mathrm{curl};\Omega) \cap H(\mathrm{div}^0;\Omega). \tag{1.1}$$

Here $\Omega \subset \mathbb{R}^2$ is a bounded polygonal domain, $(\cdot,\cdot)$ denotes the L_2 inner product, and

$$H(\mathrm{curl};\Omega) = \left\{ \boldsymbol{v} = \begin{bmatrix} v_1 \\ v_2 \end{bmatrix} \in [L_2(\Omega)]^2 : \nabla \times \boldsymbol{v} = \frac{\partial v_2}{\partial x_1} - \frac{\partial v_1}{\partial x_2} \in L_2(\Omega) \right\},$$

$$H(\mathrm{div};\Omega) = \left\{ \boldsymbol{v} = \begin{bmatrix} v_1 \\ v_2 \end{bmatrix} \in [L_2(\Omega)]^2 : \nabla \cdot \boldsymbol{v} = \frac{\partial v_1}{\partial x_1} + \frac{\partial v_2}{\partial x_2} \in L_2(\Omega) \right\},$$

$$H_0(\mathrm{curl};\Omega) = \{ \boldsymbol{v} \in H(\mathrm{curl};\Omega) : \boldsymbol{n} \times \boldsymbol{v} = 0 \text{ on } \partial\Omega \},$$

$$H(\mathrm{div}^0;\Omega) = \{ \boldsymbol{v} \in H(\mathrm{div};\Omega) : \nabla \cdot \boldsymbol{v} = 0 \},$$

where $\boldsymbol{n}$ is the unit outer normal on $\partial\Omega$.

Note that the eigenfunction $\mathring{\boldsymbol{u}}$ is subject to a divergence-free constraint, a property difficult to satisfy in numerical approximations. A common practice [4–6, 13–15, 23, 27] in designing numerical schemes for (1.1) is to neglect the divergence-free condition and instead work with the following problem:

Find $(\boldsymbol{u}, \lambda) \in H_0(\mathrm{curl};\Omega) \times \mathbb{R}$ such that $\boldsymbol{u} \neq \mathbf{0}$ and

$$(\nabla \times \boldsymbol{u}, \nabla \times \boldsymbol{v}) = \lambda(\boldsymbol{u}, \boldsymbol{v}) \quad \forall \boldsymbol{v} \in H_0(\mathrm{curl};\Omega). \tag{1.2}$$

By doing so, a non-physical zero eigenvalue, whose eigenspace is of infinite dimension, is introduced into the spectrum. This in return requires that a successful numerical Maxwell eigensolver based on (1.2), in addition to being able to approximate the physical spectrum of (1.1), must also be able to separate the numerical approximations to the non-physical zero eigenvalue from those to the physical eigenvalues. Moreover, the non-compactness of the Maxwell operator based on (1.2) poses additional complexity in the analysis of the eigensolvers.

In this paper we work directly with (1.1). The eigensolvers we will present are closely related to the numerical schemes for the following curl-curl problem:

Given $\boldsymbol{f} \in [L_2(\Omega)]^2$, find $\mathring{\boldsymbol{u}} \in H_0(\mathrm{curl};\Omega) \cap H(\mathrm{div}^0;\Omega)$ such that

$$(\nabla \times \mathring{\boldsymbol{u}}, \nabla \times \boldsymbol{v}) + \alpha(\mathring{\boldsymbol{u}}, \boldsymbol{v}) = (\boldsymbol{f}, \boldsymbol{v}) \quad \forall \boldsymbol{v} \in H_0(\mathrm{curl};\Omega) \cap H(\mathrm{div}^0;\Omega), \tag{1.3}$$

where $\alpha \in \mathbb{R}$.

When $\alpha = -\kappa^2$ with real wave number κ, the curl-curl problem (1.3) becomes the time-harmonic (frequency-domain) Maxwell equations formulated on $H_0(\mathrm{curl};\Omega) \cap H(\mathrm{div}^0;\Omega)$, and it was solved in [8] by a locally divergence-free nonconforming finite element method. The extension of the results in [8] to the case where $\alpha > 0$ is straight-forward.

In [9, 10], two other schemes were proposed for solving the curl-curl problem (1.3). One is a locally divergence-free interior penalty method [9], and the other is a nonconforming

finite element method that penalizes the divergence of the discrete solution [10]. Optimal order error estimates in both the L_2 norm and the energy norm have been established for all three schemes in [8–10]. These schemes naturally define three numerical eigensolvers for (1.1), and the main goal of this paper is to study these eigensolvers analytically and numerically. A main feature of these solvers is that they are based on the formulation (1.1) instead of the formulation (1.2), and hence they are free of zero and nonzero spurious eigenmodes. The compactness of the underlying operator also greatly simplifies the analysis of these eigensolvers. Moreover these eigensolvers do not involve choosing any penalty parameters.

We have carried out numerical experiments that demonstrate the performance and the relative merits of these eigensolvers. Furthermore, we have conducted numerical tests to illustrate the roles played by various terms in the formulation of the solvers.

It turns out that some variants of the proposed eigensolvers generate spurious eigenmodes, and we have been able to detect them by certain numerical techniques. The related numerical tests, which may be of interest for other eigensolvers that generate spurious eigenmodes, are also reported.

The rest of the paper is organized as follows. The three eigensolvers are introduced in Sect. 2, and the optimal order convergence of these eigensolvers is established in Sect. 3. Results of a series of numerical experiments on the eigensolvers are reported in Sect. 4, and we discuss in Sect. 5 some numerical tests for the detection of spurious eigenmodes. We end with some concluding remarks in Sect. 6.

2 Numerical Schemes

We formulate three Maxwell eigensolvers for (1.1) in this section.

Let $\mathcal{T}_h$ be a simplicial triangulation of Ω. We denote a triangular element by T, the diameter of T by h_T, an edge by e, and the midpoint and length of e by m_e and $|e|$. The set of the edges of the triangles in $\mathcal{T}_h$ is denoted by $\mathcal{E}_h$, and the set of the interior edges is denoted by $\mathcal{E}_h^i$. In order for the schemes to achieve optimal convergence for approximating the eigenvalues and eigenspaces, the triangulation $\mathcal{T}_h$ must be properly graded around the corners of Ω. We assume the following condition is satisfied by $\mathcal{T}_h$:

$$h_T \approx h\Phi_\mu(T) \quad \forall T \in \mathcal{T}_h. \tag{2.1}$$

Here h is the characteristic mesh size (one can take h to be the largest diameter of $T \in \mathcal{T}_h$, and some other choices of h can be found in Sect. 4) and the weight $\Phi_\mu(T)$ is defined by

$$\Phi_\mu(T) = \prod_{l=1}^{L} |c_l - c_T|^{1-\mu_l}, \tag{2.2}$$

where c_T is the center of T, and μ_l is the grading parameter chosen for each corner c_l of Ω with interior angle ω_l according to the following rules:

$$\mu_l = 1 \quad \text{if } \omega_l \le \frac{\pi}{2}, \tag{2.3a}$$

$$\mu_l < \frac{\pi}{2\omega_l} \quad \text{if } \omega_l > \frac{\pi}{2}. \tag{2.3b}$$

For any $e \subset \partial T$, the following weight is equivalent to $\Phi_\mu(T)$:

$$\Phi_\mu(e) = \prod_{l=1}^{L} |c_l - m_e|^{1-\mu_l}.$$

Remark 2.1 The choices for the grading parameters are dictated by the singularities of the solution $\overset{\circ}{\boldsymbol{u}}$ of (1.1) and (1.3) around the corner c_l of Ω [2, 19, 20]. According to (2.3) grading is needed at any corner c_l where the interior angle ω_l is larger than $\frac{\pi}{2}$. This is different from problems involving the Laplace operator where grading is only needed at re-entrant corners, and it is due to the fact that the singularities of the curl-curl operator are one order worse than the singularities of the Laplace operator.

Since the jumps of vector fields across the edges of $\mathcal{T}_h$ play an important role in the numerical schemes, we introduce the following notation: given a piecewise defined vector field $\boldsymbol{v}$, for any $e \in \mathcal{E}_h^i$ shared by two triangles T_1 and T_2 with unit normals $\boldsymbol{n}_1$ and $\boldsymbol{n}_2$ of e pointing towards the outside of T_1 and T_2 respectively, we define

$$[\![\boldsymbol{v}]\!]_t = [\![\boldsymbol{n} \times \boldsymbol{v}]\!] = (\boldsymbol{n}_1 \times \boldsymbol{v}_{T_1})|_e + (\boldsymbol{n}_2 \times \boldsymbol{v}_{T_2})|_e,$$
$$[\![\boldsymbol{v}]\!]_n = [\![\boldsymbol{n} \cdot \boldsymbol{v}]\!] = (\boldsymbol{n}_1 \cdot \boldsymbol{v}_{T_1})|_e + (\boldsymbol{n}_2 \cdot \boldsymbol{v}_{T_2})|_e.$$

Here $\boldsymbol{v}_T = \boldsymbol{v}|_T$, and we will refer to $[\![\boldsymbol{v}]\!]_t$ and $[\![\boldsymbol{v}]\!]_n$ as the tangential jump and the normal jump respectively.

For an edge e along $\partial\Omega$, we take $\boldsymbol{n}_e$ to be the unit normal of e pointing towards the outside of Ω and define

$$[\![\boldsymbol{v}]\!]_t = [\![\boldsymbol{n} \times \boldsymbol{v}]\!] = (\boldsymbol{n}_e \times \boldsymbol{v})|_e.$$

We also denote the piecewise defined curl operator and div operator by $\nabla_h \times$ and $\nabla_h \cdot$ respectively, i.e.,

$$(\nabla_h \times \boldsymbol{v})|_T = \nabla \times (\boldsymbol{v}|_T), \qquad (\nabla_h \cdot \boldsymbol{v})|_T = \nabla \cdot (\boldsymbol{v}|_T).$$

We will use the following finite element spaces for the Maxwell eigensolvers. The first is the space W_h of Crouzeix-Raviart [21] non-conforming P_1 vector fields:

$$W_h = \{\boldsymbol{v} \in [L_2(\Omega)]^2 : \boldsymbol{v}_T \in [P_1(T)]^2 \ \forall T \in \mathcal{T}_h, \boldsymbol{v} \text{ is continuous at}$$
$$\text{the midpoints of the interior edges of } \mathcal{T}_h, \text{ and } \boldsymbol{n} \times \boldsymbol{v} = 0$$
$$\text{at the midpoints of the edges of } \mathcal{T}_h \text{ along } \partial\Omega\}.$$

The second is the space V_h of locally divergence-free Crouzeix-Raviart non-conforming P_1 vector fields:

$$V_h = \{\boldsymbol{v} \in W_h : \nabla \cdot \boldsymbol{v}_T = 0 \ \forall T \in \mathcal{T}_h\}.$$

The third is the space U_h of locally divergence-free piecewise (discontinuous) P_1 vector fields:

$$U_h = \{\boldsymbol{v} \in [L_2(\Omega)]^2 : \boldsymbol{v}_T \in [P_1(T)]^2 \text{ and } \nabla \cdot \boldsymbol{v}_T = 0 \ \forall T \in \mathcal{T}_h\}.$$

We are now ready to define the three numerical eigensolvers for (1.1).

Eigensolver 1 Find $(\mathring{\boldsymbol{u}}_h, \lambda_h) \in V_h \times \mathbb{R}$ such that $\mathring{\boldsymbol{u}}_h \neq \mathbf{0}$ and

$$a_{h,0}(\mathring{\boldsymbol{u}}_h, \boldsymbol{v}) = \lambda_h(\mathring{\boldsymbol{u}}_h, \boldsymbol{v}), \quad \forall \boldsymbol{v} \in V_h, \tag{2.4}$$

where the bilinear form $a_{h,0}(\boldsymbol{w}, \boldsymbol{v})$ is defined by

$$\begin{aligned} a_{h,0}(\boldsymbol{w}, \boldsymbol{v}) = (\nabla_h \times \boldsymbol{w}, \nabla_h \times \boldsymbol{v}) &+ \sum_{e \in \mathcal{E}_h} \frac{[\Phi_\mu(e)]^2}{|e|} \int_e [\![\boldsymbol{w}]\!]_t [\![\boldsymbol{v}]\!]_t \, ds \\ &+ \sum_{e \in \mathcal{E}_h^i} \frac{[\Phi_\mu(e)]^2}{|e|} \int_e [\![\boldsymbol{w}]\!]_n [\![\boldsymbol{v}]\!]_n \, ds. \end{aligned} \tag{2.5}$$

Eigensolver 2 Find $(\mathring{\boldsymbol{u}}_h, \lambda_h) \in W_h \times \mathbb{R}$ such that $\mathring{\boldsymbol{u}}_h \neq \mathbf{0}$ and

$$b_{h,0}(\mathring{\boldsymbol{u}}_h, \boldsymbol{v}) = \lambda_h(\mathring{\boldsymbol{u}}_h, \boldsymbol{v}), \quad \forall \boldsymbol{v} \in W_h, \tag{2.6}$$

where the bilinear form $b_{h,0}(\boldsymbol{w}, \boldsymbol{v})$ is defined by

$$\begin{aligned} b_{h,0}(\boldsymbol{w}, \boldsymbol{v}) = (\nabla_h \times \boldsymbol{w}, \nabla_h \times \boldsymbol{v}) &+ \frac{1}{h^2}(\nabla_h \cdot \boldsymbol{w}, \nabla_h \cdot \boldsymbol{v}) \\ &+ \sum_{e \in \mathcal{E}_h} \frac{[\Phi_\mu(e)]^2}{|e|} \int_e [\![\boldsymbol{w}]\!]_t [\![\boldsymbol{v}]\!]_t \, ds \\ &+ \sum_{e \in \mathcal{E}_h^i} \frac{[\Phi_\mu(e)]^2}{|e|} \int_e [\![\boldsymbol{w}]\!]_n [\![\boldsymbol{v}]\!]_n \, ds. \end{aligned} \tag{2.7}$$

Eigensolver 3 Find $(\mathring{\boldsymbol{u}}_h, \lambda_h) \in U_h \times \mathbb{R}$ such that $\mathring{\boldsymbol{u}}_h \neq \mathbf{0}$ and

$$c_{h,0}(\mathring{\boldsymbol{u}}_h, \boldsymbol{v}) = \lambda_h(\mathring{\boldsymbol{u}}_h, \boldsymbol{v}), \quad \forall \boldsymbol{v} \in U_h, \tag{2.8}$$

where the bilinear form $c_{h,0}(\boldsymbol{w}, \boldsymbol{v})$ is defined by

$$\begin{aligned} c_{h,0}(\boldsymbol{w}, \boldsymbol{v}) = (\nabla_h \times \boldsymbol{w}, \nabla_h \times \boldsymbol{v}) &+ \sum_{e \in \mathcal{E}_h} \frac{[\Phi_\mu(e)]^2}{|e|} \int_e [\![\boldsymbol{w}]\!]_t [\![\boldsymbol{v}]\!]_t \, ds \\ &+ \sum_{e \in \mathcal{E}_h^i} \frac{[\Phi_\mu(e)]^2}{|e|} \int_e [\![\boldsymbol{w}]\!]_n [\![\boldsymbol{v}]\!]_n \, ds \\ &+ h^{-2} \sum_{e \in \mathcal{E}_h} \frac{1}{|e|} \int_e (\Pi_e^0 [\![\boldsymbol{w}]\!]_t)(\Pi_e^0 [\![\boldsymbol{v}]\!]_t) \, ds \\ &+ h^{-2} \sum_{e \in \mathcal{E}_h^i} \frac{1}{|e|} \int_e (\Pi_e^0 [\![\boldsymbol{w}]\!]_n)(\Pi_e^0 [\![\boldsymbol{v}]\!]_n) \, ds, \end{aligned} \tag{2.9}$$

and Π_e^0 is the L_2 orthogonal projection from $L_2(e)$ onto the space $P_0(e)$ of constant functions on e.

Remark 2.2 The following comments provide some intuitive motivations for the three Maxwell eigensolvers. More insights on various components of these schemes are provided by the numerical examples in Sect. 4.

1. Both Eigensolver 1 and Eigensolver 2 use classical nonconforming vector fields that have certain weak continuity. Eigensolver 3 is an interior penalty type discontinuous Galerkin method that uses completely discontinuous piecewise smooth vector fields. The last two terms in (2.9) compensate for the lack of any continuity in the discrete vector fields and they turn out to be necessary.
2. The divergence-free constraint in the eigenfunctions is imposed in Eigensolver 1 and Eigensolver 3 through the locally divergence-free condition in the definitions of V_h and U_h, and the same constraint is imposed in Eigensolver 2 through penalizing the divergence term in the bilinear form $b_{h,0}$. In all three solvers, certain consistency terms involving the jumps of both the normal and tangential components of the numerical solutions across element interfaces are also needed. These terms ensure that the inherent constraints for the space $H_0(\mathrm{curl};\Omega)\cap H(\mathrm{div}^0;\Omega)$ are satisfied by the discrete vector fields in a weak sense.
3. Each numerical eigensolver has its merits.
   - In terms of the computational domain: the finite element space V_h for Eigensolver 1 does not have a completely local basis when the domain is multiply connected (see Fig. 3, right); but the finite element spaces W_h and U_h for Eigensolver 2 and Eigensolver 3 have completely local bases for general domains.
   - In terms of the mesh: the weak continuity condition in the finite element spaces V_h and W_h for Eigensolver 1 and Eigensolver 2 require the meshes to be conforming; but the Eigensolver 3 can be applied to both conforming and n-irregular nonconforming meshes (see Fig. 1 and Remark 3.4).
   - In terms of the dimensions of the finite element spaces: the ratio of $\dim V_h : \dim W_h : \dim U_h$ is approximately $2:3:5$.

3 Error Analysis

In this section we give a unified error analysis for the three Maxwell eigensolvers. First we relate the Maxwell eigenproblem to the eigenproblem of a compact operator.

Given any $\boldsymbol{f}\in[L_2(\Omega)]^2$, we define $T\boldsymbol{f}\in H_0(\mathrm{curl};\Omega)\cap H(\mathrm{div}^0;\Omega)$ by the condition that

$$(\nabla\times(T\boldsymbol{f}),\nabla\times\boldsymbol{v})+(T\boldsymbol{f},\boldsymbol{v})=(\boldsymbol{f},\boldsymbol{v}) \tag{3.1}$$

for all $\boldsymbol{v}\in H_0(\mathrm{curl};\Omega)\cap H(\mathrm{div}^0;\Omega)$, i.e., $T\boldsymbol{f}$ is the solution of (1.3) with $\alpha=1$. Clearly T is a bounded linear operator from $[L_2(\Omega)]^2$ into $H_0(\mathrm{curl};\Omega)\cap H(\mathrm{div}^0;\Omega)$. Since $H_0(\mathrm{curl};\Omega)\cap H(\mathrm{div}^0;\Omega)$ is a compact subspace of $[L_2(\Omega)]^2$ (cf. [17]), the operator $T:[L_2(\Omega)]^2\longrightarrow[L_2(\Omega)]^2$ is symmetric, positive and compact. Moreover, $(\mathring{\boldsymbol{u}},\lambda)$ satisfy (1.1) if and only if

$$T\,\mathring{\boldsymbol{u}}=\frac{1}{1+\lambda}\,\mathring{\boldsymbol{u}}\,. \tag{3.2}$$

The eigenfunctions of T are precisely the Maxwell eigenfunctions.

Next we consider nonconforming approximations of T corresponding to the three schemes (2.4), (2.6) and (2.8).

Let Z_h be the finite element space V_h, U_h or W_h, and $\mathcal{N}_{h,0}(\cdot,\cdot)$ be the corresponding bilinear form $a_{h,0}(\cdot,\cdot)$, $b_{h,0}(\cdot,\cdot)$ or $c_{h,0}(\cdot,\cdot)$. The equations defining the three Maxwell eigensolvers can then be written as

$$\mathcal{N}_{h,0}(\mathring{\boldsymbol{u}}_h, \boldsymbol{v}) = \lambda_h(\mathring{\boldsymbol{u}}_h, \boldsymbol{v}) \quad \forall \boldsymbol{v} \in Z_h. \tag{3.3}$$

The discrete analog of T is the operator $T_h : [L_2(\Omega)]^2 \longrightarrow Z_h \subset [L_2(\Omega)]^2$ defined by

$$\mathcal{N}_{h,1}(T_h \boldsymbol{f}, \boldsymbol{v}) = (\boldsymbol{f}, \boldsymbol{v}) \quad \forall \boldsymbol{v} \in Z_h, \tag{3.4}$$

where

$$\mathcal{N}_{h,1}(\boldsymbol{w}, \boldsymbol{v}) = \mathcal{N}_{h,0}(\boldsymbol{w}, \boldsymbol{v}) + (\boldsymbol{w}, \boldsymbol{v}).$$

In other words $T_h \boldsymbol{f} \in Z_h$ is the nonconforming finite element approximation of the solution $T\boldsymbol{f}$ of the Maxwell source problem. Note that

$$T_h \mathring{\boldsymbol{u}}_h = \frac{1}{1+\lambda_h} \mathring{\boldsymbol{u}}_h \tag{3.5}$$

is equivalent to (3.3). The eigenfunctions of T_h are precisely the discrete Maxwell eigenfunctions.

The following discretization error estimates for the Maxwell source problem have been derived in [8–10]:

$$\|(T - T_h)\boldsymbol{f}\|_{L_2(\Omega)} \le C_\epsilon h^{2-\epsilon} \|\boldsymbol{f}\|_{L_2(\Omega)} \tag{3.6}$$

for all $\boldsymbol{f} \in [L_2(\Omega)]^2$, and

$$\|(T - T_h)\boldsymbol{f}\|_h \le C_\epsilon h^{1-\epsilon} \|\boldsymbol{f}\|_{L_2(\Omega)} \le C_\epsilon h^{1-\epsilon} \|\boldsymbol{f}\|_h \tag{3.7}$$

for all $\boldsymbol{f} \in H_0(\mathrm{curl};\Omega) \cap H(\mathrm{div}^0;\Omega) + Z_h$, where ϵ is an arbitrary positive constant and the mesh-dependent energy norm $\|\cdot\|_h$ is defined by

$$\|\boldsymbol{v}\|_h^2 = \mathcal{N}_{h,1}(\boldsymbol{v}, \boldsymbol{v}).$$

The uniform estimates (3.6) and (3.7) imply that the classical theory of spectral approximation [3, 16, 24] can be applied to the nonconforming Maxwell eigensolvers.

Theorem 3.1 *Let $0 \le \lambda_1 \le \lambda_2 \le \cdots$ be the eigenvalues of (1.1), $\lambda = \lambda_j = \lambda_{j+1} = \cdots = \lambda_{j+m-1}$ be an eigenvalue with multiplicity m, and $Z_\lambda \subset H_0(\mathrm{curl};\Omega) \cap H(\mathrm{div}^0;\Omega)$ be the corresponding m dimensional eigenspace. Let $0 \le \lambda_{h,1} \le \lambda_{h,2} \le \cdots$ be the eigenvalues obtained by one of the three eigensolvers. Then as $h \downarrow 0$, we have*

$$|\lambda_{h,l} - \lambda| \le C_{\lambda,d_\lambda,\epsilon} h^{2-\epsilon}, \quad l = j, j+1, \ldots, j+m-1, \tag{3.8}$$

where d_λ is the distance from λ to the other Maxwell eigenvalues and ϵ is an arbitrary positive number.

Furthermore, if $Z_{h,\lambda}$ is the space spanned by the discrete Maxwell eigenfunctions corresponding to $\lambda_{h,j}, \ldots, \lambda_{h,j+m-1}$, then the gap between Z_λ and $Z_{h,\lambda}$ goes to zero at the rate of $C_{\lambda,d_\lambda,\epsilon} h^{2-\epsilon}$ in the L_2 norm and at the rate of $C_{\lambda,d_\lambda,\epsilon} h^{1-\epsilon}$ in the energy norm $\|\cdot\|_h$.

Proof Let $1 \geq \mu_1 \geq \mu_2 \geq \cdots$ be the eigenvalues of T and $1 \geq \mu_{h,1} \geq \mu_{h,2} \geq \cdots$ be the eigenvalues of T_h. In view of the relations (3.2) and (3.5), it is equivalent to establish the convergence of $\mu_{h,j}$ to μ_j.

Let μ be an eigenvalue of T of multiplicity m corresponding to the Maxwell eigenvalue λ. The L_2 orthogonal projection E_μ onto the eigenspace $Z_\mu = Z_\lambda$ is given by the contour integral [22]

$$E_\mu = \frac{1}{2\pi i} \int_{C_{\mu,\delta_\mu}} (\zeta I - T)^{-1} d\zeta, \tag{3.9}$$

where I is the identity operator on $[L_2(\Omega)]^2$, C_{μ,δ_μ} is the counterclockwise oriented circle centered at μ with radius δ_μ, and δ_μ is small enough so that μ is the only eigenvalue of T inside and on C_{μ,δ_μ}.

For h sufficiently small, the operator $\zeta I - T_h$ is invertible on C_{μ,δ_μ} and we can define the L_2 orthogonal projection $E_{h,\mu}$ by

$$E_{h,\mu} = \frac{1}{2\pi i} \int_{C_{\mu,\delta_\mu}} (\zeta I - T_h)^{-1} d\zeta. \tag{3.10}$$

The space $Z_{h,\mu} = Z_{h,\lambda} = E_{h,\mu}[L_2(\Omega)]^2$ is spanned by the eigenfunctions of T_h corresponding to eigenvalues of T_h inside C_{μ,δ_μ}.

It follows from (3.6), (3.9) and (3.10) that

$$\|(E_\lambda - E_{h,\lambda})\boldsymbol{w}\|_{L_2(\Omega)} \leq C_{\delta_\mu,\epsilon} h^{2-\epsilon} \|\boldsymbol{w}\|_{L_2(\Omega)} \tag{3.11}$$

for all $\boldsymbol{w} \in [L_2(\Omega)]^2$ and

$$\|(E_\lambda - E_{h,\lambda})\boldsymbol{w}\|_h \leq C_{\delta_\mu,\epsilon} h^{1-\epsilon} \|\boldsymbol{w}\|_h \tag{3.12}$$

for all $\boldsymbol{w} \in H_0(\mathrm{curl};\Omega) \cap H(\mathrm{div}^0;\Omega) + Z_h$.

Hence, for h sufficiently small, the rank of $E_{h,\mu}$ is m and there are exactly m eigenvalues (counting multiplicity) of T_h inside the circle C_{μ,δ_μ}. To complete the proof of the first part of the theorem, it only remains to estimate $|\mu - \mu_h|$, where μ_h is any one of the eigenvalues of T_h inside C_{μ,δ_μ}.

Let $\boldsymbol{x} \in Z_{h,\lambda}$ be a unit eigenfunction of μ_h. Then we have

$$(T_h \boldsymbol{x}, \boldsymbol{x}) = \mu_h \quad \text{and} \quad \|\boldsymbol{x}\|_{L_2(\Omega)} = 1. \tag{3.13}$$

Let $\hat{\boldsymbol{x}} = E_\lambda \boldsymbol{x}$ and $\hat{\boldsymbol{y}} = \boldsymbol{x} - \hat{\boldsymbol{x}}$. Then $\hat{\boldsymbol{x}}$ and $\hat{\boldsymbol{y}}$ are orthogonal with respect to both the L_2 inner product and the inner product $(T\cdot,\cdot)$, and the estimate (3.11) implies that

$$\|\hat{\boldsymbol{y}}\|_{L_2(\Omega)} = \|(E_\lambda - E_{h,\lambda})\boldsymbol{x}\|_{L_2(\Omega)} \leq C_{\delta_\mu,\epsilon} h^{2-\epsilon}. \tag{3.14}$$

Hence it follows from Pythagoras' theorem with respect to the L_2 inner product that

$$1 - \|\hat{\boldsymbol{x}}\|^2_{L_2(\Omega)} = \|\boldsymbol{x}\|^2_{L_2(\Omega)} - \|\hat{\boldsymbol{x}}\|^2_{L_2(\Omega)} = \|\hat{\boldsymbol{y}}\|^2_{L_2(\Omega)} \leq C_{\delta_\mu,\epsilon} h^{4-\epsilon}. \tag{3.15}$$

In particular we have $\hat{\boldsymbol{x}} \neq \boldsymbol{0}$ for h sufficiently small.

Let $\hat{\boldsymbol{e}} = \hat{\boldsymbol{x}}/\|\hat{\boldsymbol{x}}\|_{L_2(\Omega)}$. Then $\hat{\boldsymbol{e}}$ is a unit eigenfunction of T for the eigenvalue μ, and we have, by (3.13),

$$\begin{aligned} |\mu - \mu_h| &= \big|(T\hat{\boldsymbol{e}}, \hat{\boldsymbol{e}}) - (T_h\boldsymbol{x}, \boldsymbol{x})\big| \\ &\le \big|((T - T_h)\boldsymbol{x}, \boldsymbol{x})\big| + \big|(T\hat{\boldsymbol{e}}, \hat{\boldsymbol{e}}) - (T\boldsymbol{x}, \boldsymbol{x})\big|. \end{aligned} \tag{3.16}$$

From (3.6) we have

$$\big|((T - T_h)\boldsymbol{x}, \boldsymbol{x})\big| \le C_\epsilon h^{2-\epsilon}, \tag{3.17}$$

and it follows from Pythagoras' theorem with respect to the inner product $(T\cdot, \cdot)$ that

$$\begin{aligned} \big|(T\hat{\boldsymbol{e}}, \hat{\boldsymbol{e}}) - (T\boldsymbol{x}, \boldsymbol{x})\big| &= \big|(T\hat{\boldsymbol{e}}, \hat{\boldsymbol{e}}) - (T\hat{\boldsymbol{x}}, \hat{\boldsymbol{x}}) - (T\hat{\boldsymbol{y}}, \hat{\boldsymbol{y}})\big| \\ &\le (1 - \|\hat{\boldsymbol{x}}\|^2_{L_2(\Omega)})(T\hat{\boldsymbol{e}}, \hat{\boldsymbol{e}}) + (T\hat{\boldsymbol{y}}, \hat{\boldsymbol{y}}). \end{aligned} \tag{3.18}$$

Combining (3.14), (3.15) and (3.18), we find

$$\big|(T\hat{\boldsymbol{e}}, \hat{\boldsymbol{e}}) - (T\boldsymbol{x}, \boldsymbol{x})\big| \le C_{\delta_\mu, \epsilon} h^{4-\epsilon},$$

which together with (3.16) and (3.17) implies

$$|\mu - \mu_h| \le C_{\delta_\mu, \epsilon} h^{2-\epsilon}. \tag{3.19}$$

The estimate (3.8) follows from (3.19) and the relations

$$\mu_j = 1/(1 + \lambda_j) \quad \text{and} \quad \mu_{h,j} = 1/(1 + \lambda_{h,j}).$$

Finally, we recall that the gap $\hat{\delta}(M, N)$ between two subspaces M and N of a normed linear space $(X, \|\cdot\|_X)$ is defined by (cf. [24])

$$\hat{\delta}(M, N) = \max(\delta(M, N), \delta(N, M)),$$

where

$$\delta(M, N) = \sup_{\substack{x \in M \\ \|x\|_X = 1}} \inf_{y \in N} \|x - y\|_X.$$

Therefore the statements about the gap between $Z_\lambda = Z_\mu$ and $Z_{h,\lambda} = Z_{h,\mu}$ follow immediately from (3.11) and (3.12). □

Remark 3.2 Because of the graded mesh, the error estimates in Theorem 3.1 are optimal even when the Maxwell eigenfunctions do not have full regularity, which may happen when one of the interior angles of the computational domain is larger than $\frac{\pi}{2}$.

Remark 3.3 The compactness of the solution operator T and the existence of the uniform estimates (3.6) and (3.7) greatly simplify the analysis of the three nonconforming Maxwell eigensolvers. In comparison the analysis of Maxwell eigensolvers [4–6, 13–15] based on (1.2) is much more involved.

Remark 3.4 The error estimates in Theorem 3.1 hold for Eigensolver 3 when it is applied to both conforming meshes and n-irregular nonconforming meshes (see Fig. 1 for an example of 1-irregular mesh, or [12] for an example of a 3-irregular mesh). For more general nonconforming meshes, our solvers can not ensure a spurious-free spectrum. A similar phenomenon was discussed in [12] when the standard symmetric interior penalty method [1] based on (1.2) is used to approximate the Maxwell eigenvalues.

4 Numerical Results

In this section we report the results of a series of numerical experiments on the three nonconforming Maxwell eigensolvers. They confirm the theoretical results, demonstrate the relative merits of each eigensolver, and illustrate the roles played by various terms in the formulations of the eigensolvers.

The following examples are considered throughout this section:

Example 1 We take the computational domain to be the square

$$\Omega = (0, \pi)^2.$$

The exact Maxwell eigenvalues on this domain are given by $r^2 + s^2$, where $r, s = 0, 1, 2, 3, 4, \ldots$ and $r^2 + s^2 > 0$. For instance, the first 10 eigenvalues are 1, 1, 2, 4, 4, 5, 5, 8, 9, 9. The eigenfunctions are H^2 functions.

Example 2 We take the computational domain to be the L-shaped domain (Fig. 3, left)

$$\Omega = (-0.5, 0.5)^2 \setminus [0, 0.5]^2.$$

Based on Dauge's benchmark examples for the Maxwell eigenproblem (http://perso.univ-rennes1.fr/monique.dauge/core/index.html), the values of the first 5 eigenvalues are 5.90248729632, 14.13612546712, 39.47841760436, 39.47841760436 and 45.5579175916. It is also known from the same source that the 1st and 5th Maxwell eigenfunctions have a strong unbounded singularity, the 2nd one belongs to $H^1(\Omega)$, and the 3rd and the 4th ones are analytic.

Example 3 We take the computational domain to be the doubly connected domain (Fig. 3, right)

$$\Omega = (0, 4)^2 \setminus [1, 3]^2.$$

The smallest Maxwell eigenvalue on this domain is 0 with multiplicity 1. The corresponding eigenfunction is defined by $\boldsymbol{u} = \nabla\phi$, where $\phi \in H^1(\Omega)$ satisfies

$$-\Delta\phi = 0 \quad \text{in } \Omega,$$
$$\phi|_{\Gamma_{int}} = 0, \qquad \phi|_{\Gamma_{ext}} = 1,$$

and Γ_{int} (resp. Γ_{ext}) is the boundary of $[1, 3]^2$ (resp. $[0, 4]^2$).

The characteristic mesh size h for the numerical experiments is chosen as follows. For Example 1, we take $h = \pi/n$, where n is the number of the subintervals along

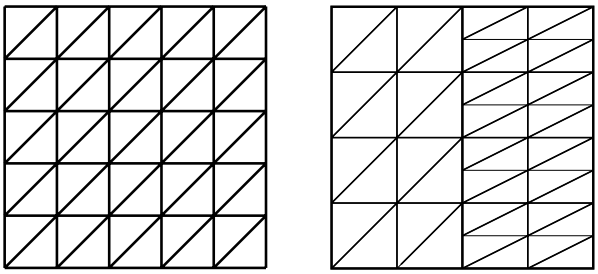

Fig. 1 Conforming uniform mesh (*left*) and 1-irregular nonconforming mesh (*right*) on the square domain $(0, \pi)^2$

$[0, \pi] \times \{y = 0\}$, for the conforming and nonconforming meshes in Fig. 1. For Example 2, we take $h = 1/(2n)$, where n is the number of the subintervals along $[-0.5, 0] \times \{y = 0.5\}$, for the mesh in Fig. 3 (left). For Example 3, we take $h = 4/n$, where n is the number of the subintervals along $[0, 4] \times \{y = 0\}$, for the mesh in Fig. 3 (right).

In all the plots, the symbol "o" denotes the exact eigenvalue, and "(2)" indicates that the multiplicity of the eigenvalue is 2. When more than one numerical eigenvalue on different mesh resolutions is reported in the same plot, we use different color and/or symbol codings to represent the results based on the nondecreasing ordering of the numerical eigenvalues. Some extra care would be needed when one reads these plots especially when there is the occurrence of eigenvalue crossing, for instance in Figs. 8, 10, and 13–16.

4.1 Numerical Results for Eigensolver 1

In this subsection we present numerical results on the accuracy of the Eigensolver 1 and on the roles played by the consistency terms.

4.1.1 Accuracy of the Scheme

In the first experiment we compute the Maxwell eigenvalues on the square $(0, \pi)^2$ using the uniform meshes depicted in Fig. 1 (left).

We plot the first 20 numerical eigenvalues versus the parameter $n = \pi/h$ in Fig. 2, from which one can see that the eigenvalues are well resolved even when the meshes are still coarse and there is no spurious eigenmode. The numerical approximations converge with second order accuracy which confirms the error estimate (3.8). To save space, only the first 5 numerical eigenvalues and their convergence rates are included in Table 1.

In the second experiment we compute the Maxwell eigenvalues for the L-shaped domain $(-0.5, 0.5)^2 \setminus [0, 0.5]^2$ using the graded meshes depicted in Fig. 3 (left), where the grading parameter at the re-entrant corner is chosen to be $\frac{1}{3}$.

Table 2 contains the numerical results for the first 5 Maxwell eigenvalues. One can see that our method has second order accuracy, on relatively coarse meshes and for eigenfunctions with very different regularity. In Fig. 4 we plot the first 10 numerical eigenvalues versus $n = 1/(2h)$, which clearly demonstrates the absence of any spurious eigenmodes.

4.1.2 The Role of the Consistency Terms

In order for a numerical scheme to be successful for either the Maxwell source problem or the Maxwell eigenproblem, the correct amount of continuity for the tangential and/or the normal component of the discrete vector fields must be imposed across element interfaces. If the continuity is over-imposed, the scheme may generate a sequence of approximations that

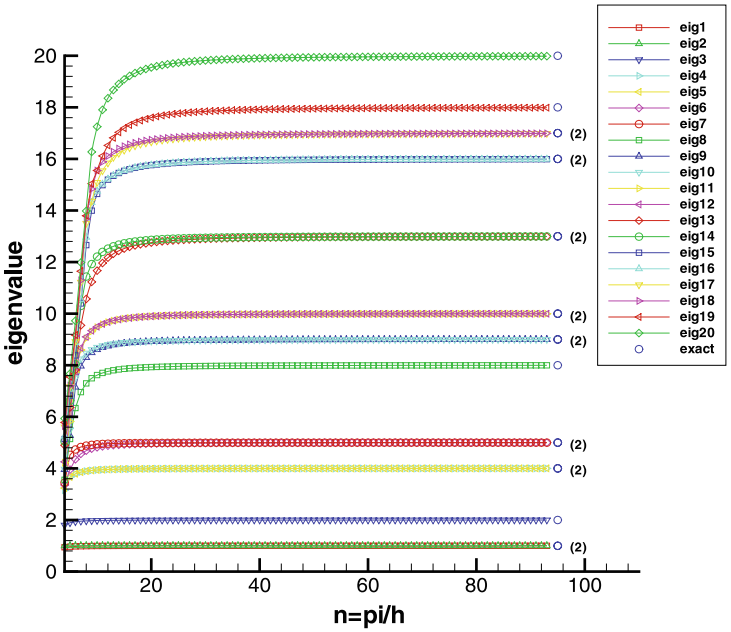

Fig. 2 First 20 Maxwell eigenvalues computed by Eigensolver 1 on $(0,\pi)^2$ with conforming uniform meshes

Table 1 First 5 Maxwell eigenvalues computed by Eigensolver 1 on $(0,\pi)^2$ with conforming uniform meshes

$n=\frac{\pi}{h}$	1st	Order	2nd	Order	3rd	Order	4th	Order	5th	Order
4	0.943	–	1.000	–	1.800	–	3.154	–	3.238	–
8	0.988	2.19	1.000	−0.67	1.967	2.60	3.895	3.01	3.896	2.87
16	0.997	2.07	1.000	1.26	1.993	2.26	3.977	2.21	3.977	2.20
32	0.999	2.03	1.000	1.72	1.998	2.11	3.995	2.08	3.995	2.08
64	1.000	2.01	1.000	1.87	2.000	2.05	3.999	2.03	3.999	2.03
128	1.000	2.01	1.000	1.94	2.000	2.03	4.000	2.01	4.000	2.01
Exact	1		1		2		4		4	

converge to a wrong solution [5, 25]. On the other hand, if the continuity is under-imposed, the scheme may not converge [8]. In this subsection we will demonstrate numerically that the correct amount of continuity is imposed by Eigensolver 1.

For this purpose we rewrite the bilinear form $a_{h,0}(\boldsymbol{w},\boldsymbol{v})$ as

$$a_{h,0}(\boldsymbol{w},\boldsymbol{v}) = (\nabla_h\times\boldsymbol{w},\nabla_h\times\boldsymbol{v}) + C_{p,t}\sum_{e\in\mathcal{E}_h}\frac{[\Phi_\mu(e)]^2}{|e|}\int_e [\![\boldsymbol{w}]\!]_t[\![\boldsymbol{v}]\!]_t\,ds$$
$$+ C_{p,n}\sum_{e\in\mathcal{E}_h^i}\frac{[\Phi_\mu(e)]^2}{|e|}\int_e [\![\boldsymbol{w}]\!]_n[\![\boldsymbol{v}]\!]_n\,ds, \tag{4.1}$$

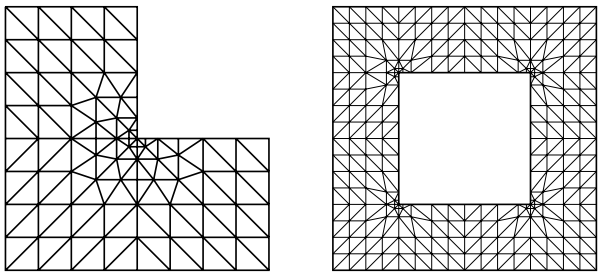

Fig. 3 Graded meshes on the L-shaped domain $(-0.5, 0.5)^2 \setminus [0, 0.5]^2$ (*left*) and on the doubly connected domain $(0, 4)^2 \setminus [1, 3]^2$ (*right*)

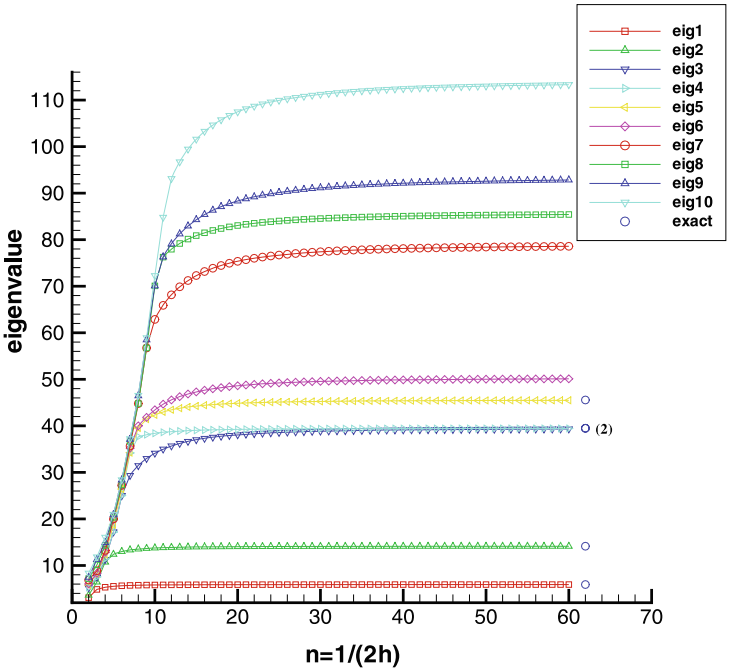

Fig. 4 First 10 Maxwell eigenvalues computed by Eigensolver 1 on the L-shaped domain using graded meshes

Table 2 First 5 Maxwell eigenvalues computed by Eigensolver 1 on the L-shaped domain using graded meshes

$n = \frac{1}{2h}$	1st	Order	2nd	Order	3rd	Order	4th	Order	5th	Order
4	5.319	–	10.727	–	11.276	–	11.441	–	12.350	–
8	5.756	1.99	13.532	2.50	31.448	1.81	37.652	3.94	39.529	2.46
16	5.867	2.05	13.992	2.07	37.307	1.89	39.100	2.27	44.429	2.42
32	5.894	2.08	14.101	2.03	38.929	1.98	39.390	2.10	45.291	2.08
64	5.901	2.09	14.127	2.01	39.341	2.00	39.457	2.05	45.493	2.03
Exact	5.902		14.136		39.478		39.478		45.558	

where we take $C_{p,n} = C_{p,t} = 1$ in (2.5). Here $\sum_{e\in\mathcal{E}_h} \frac{[\Phi_\mu(e)]^2}{|e|} \int_e [\![\boldsymbol{w}]\!]_t [\![\boldsymbol{v}]\!]_t ds$ is a consistency term involving the *tangential* jumps of the discrete vector fields across element interfaces, and $\sum_{e\in\mathcal{E}_h^i} \frac{[\Phi_\mu(e)]^2}{|e|} \int_e [\![\boldsymbol{w}]\!]_n [\![\boldsymbol{v}]\!]_n ds$ is a consistency term involving the *normal* jumps.

From Fig. 5 we see that if we simply remove either the tangential consistency term or the normal one from our solver, i.e., if we take $C_{p,n} = 0, C_{p,t} = 1$ (T-type variant) or $C_{p,n} = 1, C_{p,t} = 0$ (N-type variant) in (4.1), then spurious eigenmodes will appear. In particular, zero spurious eigenmodes are generated by the N-type variant. Similar results are also observed on the L-shaped domain.

We have also tested the effects of different choices of the parameters $C_{p,n}$ and $C_{p,t}$ on the performance of the eigensolver on the square $(0, \pi)^2$. From the plots in Fig. 6 we can see that the performance of the eigensolver containing both consistency terms (TN-type variant) relatively is not sensitive to the values of $C_{p,n}$ and $C_{p,t}$. On the other hand the performance of the T-type variant improves dramatically with a large $C_{p,t}$. The lower range of the spectrum is well-captured (indeed with second order accuracy). However, some nonzero spurious eigenvalues still exist for a fixed $C_{p,t}$. The performance of the N-type variant also improves with a larger $C_{p,n}$. But many spurious eigenmodes still persist.

We have carried out similar experiments for the L-shaped domain using graded meshes. From the plots in Fig. 7 we see that both the T-type and the N-type variants perform well for relatively large parameters $C_{p,t}$ and $C_{p,n}$, though the N-type variant still produces 3 spurious zero eigenvalues.

From the numerical study we can conclude that Eigensolver 1 imposes the correct amount of continuity through the two consistency terms and it does not involve any penalty parameters. In addition, the tangential consistency term is necessary for removing the zero spurious eigenmodes, and a larger $C_{p,t}$ (resp. $C_{p,n}$) in (4.1) can improve the performance of the T-type (resp. N-type) variant of Eigensolver 1.

In Sect. 5 we will present some numerical techniques that can detect the spurious eigenmodes generated by the T-type and N-type variants.

4.2 Numerical Results for Eigensolver 2

In this subsection we present numerical results for Eigensolver 2. We will focus on the accuracy of the scheme, the role of the weight for the divergence term in $b_{h,0}(\cdot,\cdot)$, and the performance of the scheme for the doubly connected domain. Results similar to those reported in Sect. 4.1.2 for Eigensolver 1 also holds for Eigensolver 2 and will not be repeated here.

4.2.1 Accuracy of the Scheme

In the first experiment we compute the Maxwell eigenvalues for the square $(0, \pi)^2$ using uniform meshes. In the top of Fig. 8, we plot the numerical results of the first 20 eigenvalues versus the parameter $n = \pi/h$, from which one can see that the eigenvalues are well resolved even for very coarse meshes and there is no spurious eigenmode. The numerical approximations converge with second order accuracy, which confirms the error estimate (3.8). To save space, only the first 5 numerical eigenvalues and their convergence rates are reported in Table 3.

In the second experiment, we compute the Maxwell eigenvalues for the L-shaped domain, where the meshes are graded around the re-entrant corner with the grading parameter $\frac{1}{3}$. Table 4 contains the first 5 numerical eigenvalues, from which one can see that the scheme has

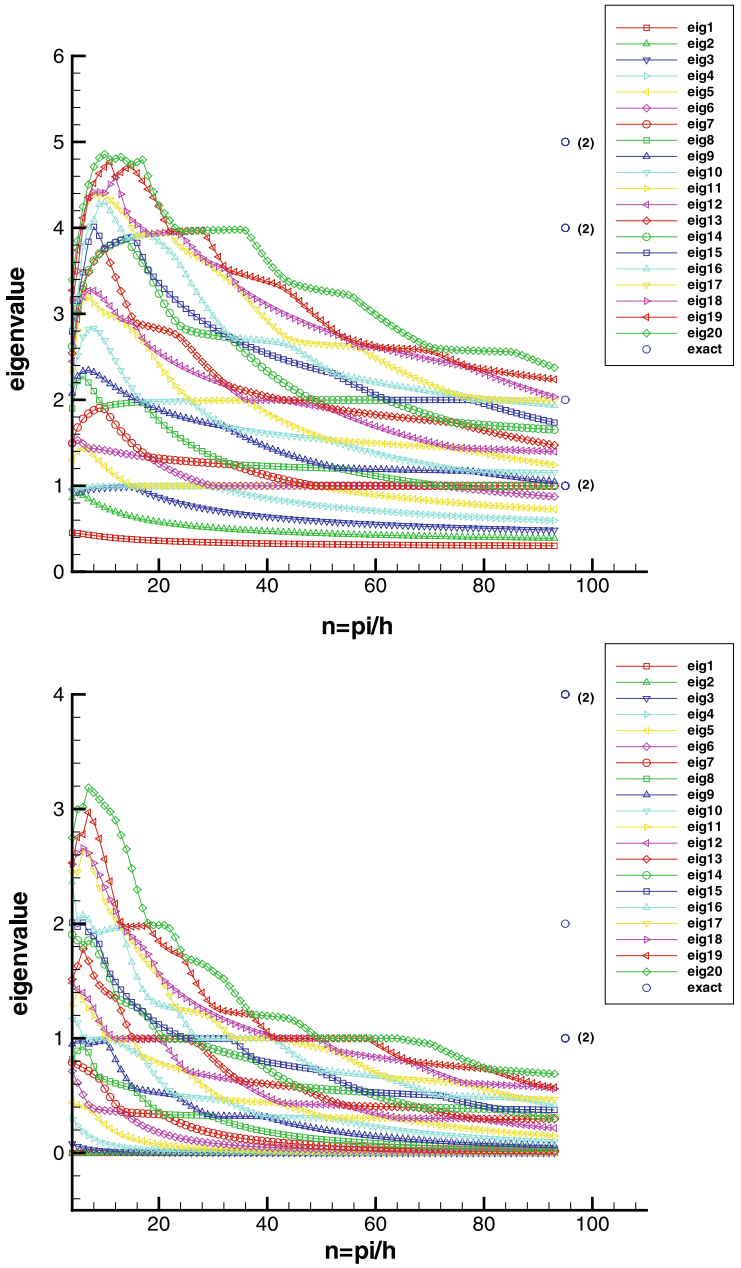

Fig. 5 Maxwell eigenvalues on $(0,\pi)^2$ computed by the *T-type* variant (*top*, $C_{p,n}=0, C_{p,t}=1$) and the *N-type* variant (*bottom*, $C_{p,n}=1, C_{p,t}=0$) of Eigensolver 1 using conforming uniform meshes

second order accuracy on relatively coarse meshes. In Fig. 9 we plot the first 10 numerical eigenvalues versus $n=1/(2h)$, which shows the absence of spurious eigenmodes.

Note that Tables 1 and 3 give almost identical results, and so do Tables 2 and 4.

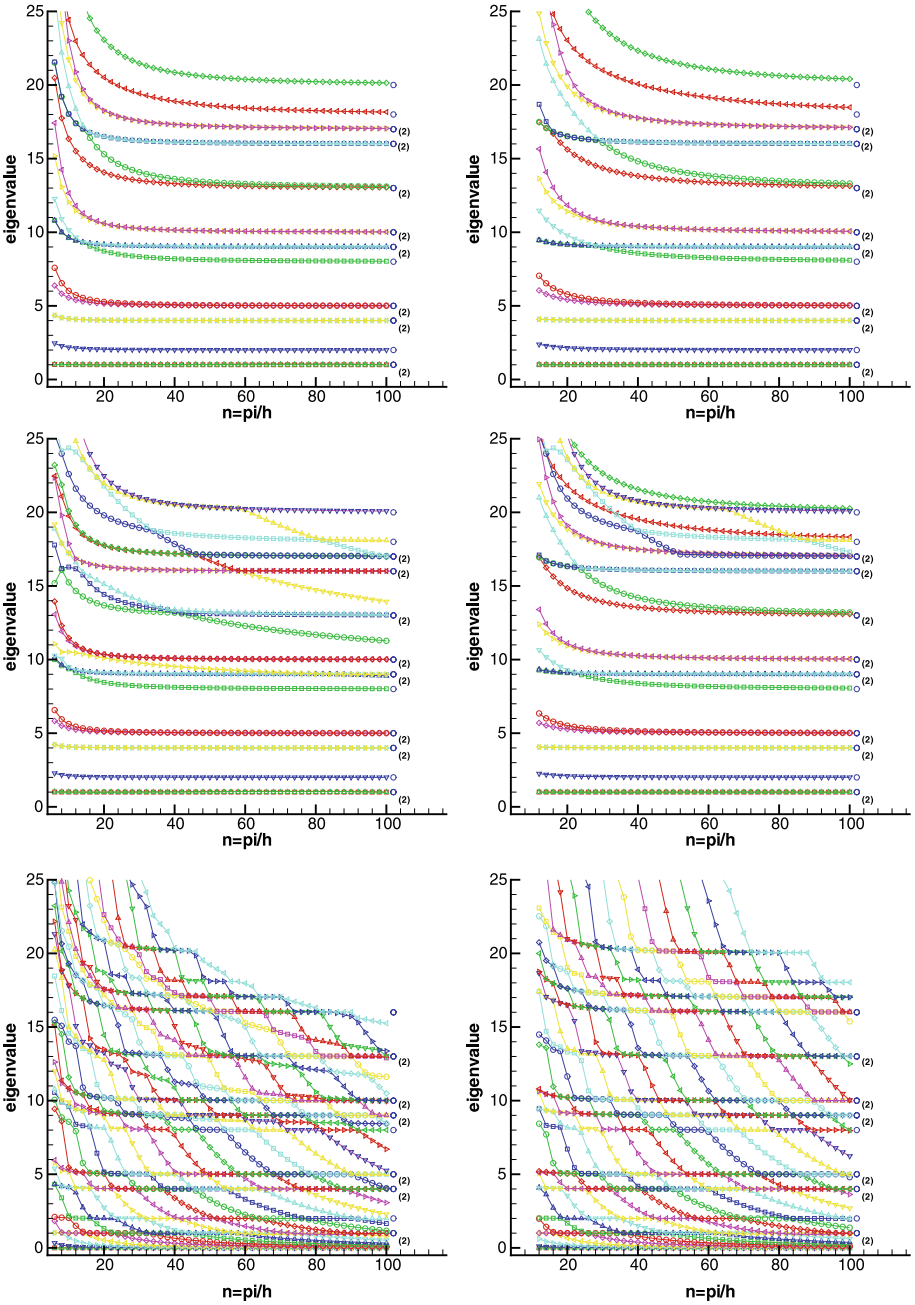

Fig. 6 Maxwell eigenvalues (from *top* to *bottom*) on $(0,\pi)^2$ computed by TN-type ($C_{p,n} = C_{p,t} = C_p$), T-type ($C_{p,n} = 0, C_{p,t} = C_p$) and N-type ($C_{p,n} = C_p, C_{p,t} = 0$) variants of Eigensolver 1 using conforming uniform meshes, where $C_p = 30$ on the *left* and $C_p = 100$ on the *right*

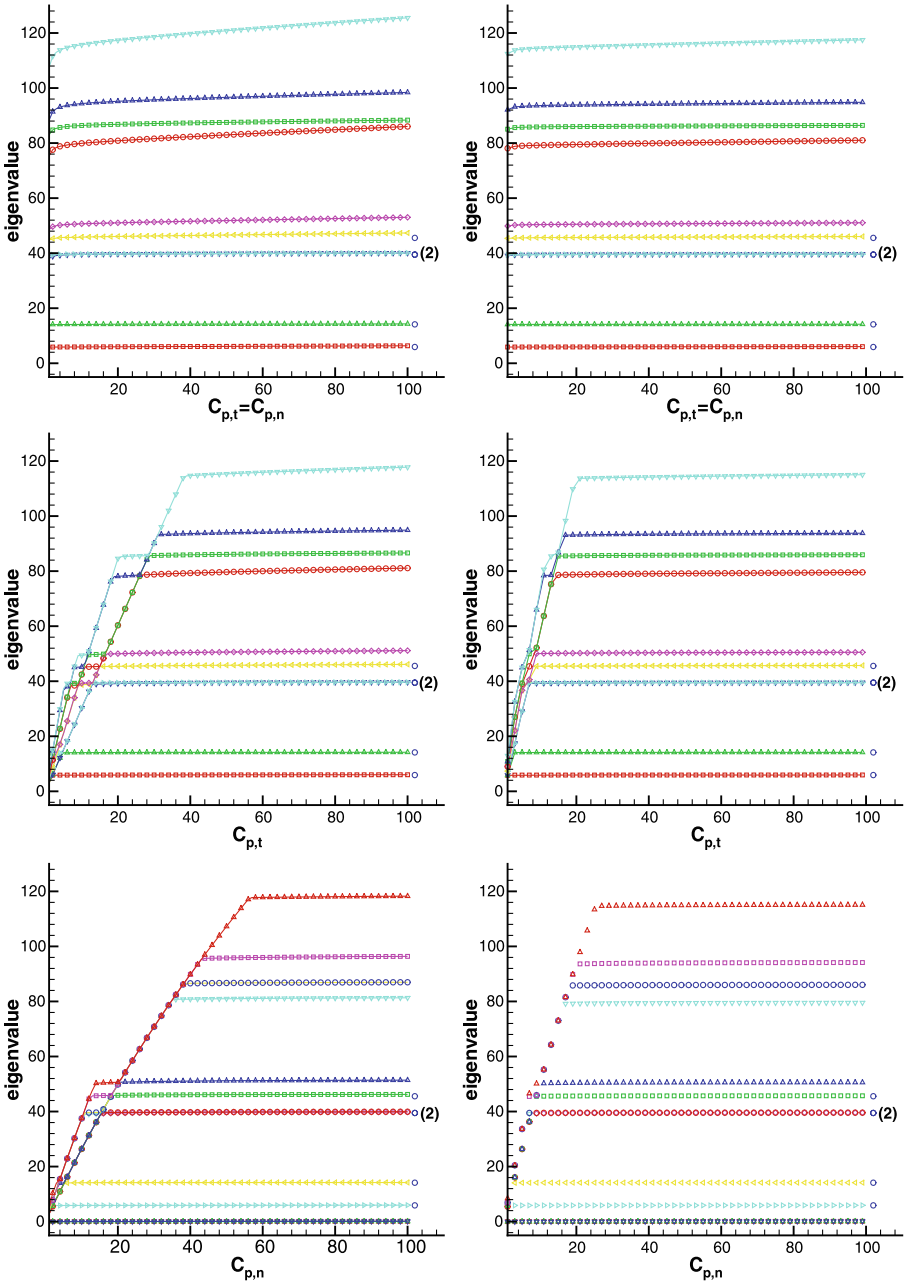

Fig. 7 Maxwell eigenvalues (from *top* to *bottom*) for the L-shaped domain computed by TN-type ($C_{p,n} = C_{p,t} = C_p$), T-type ($C_{p,n} = 0, C_{p,t} = C_p$) and N-type ($C_{p,n} = C_p, C_{p,t} = 0$) variants of Eigensolver 1 using graded meshes, where $C_p = 25$ on the *left* and $C_p = 50$ on the *right*

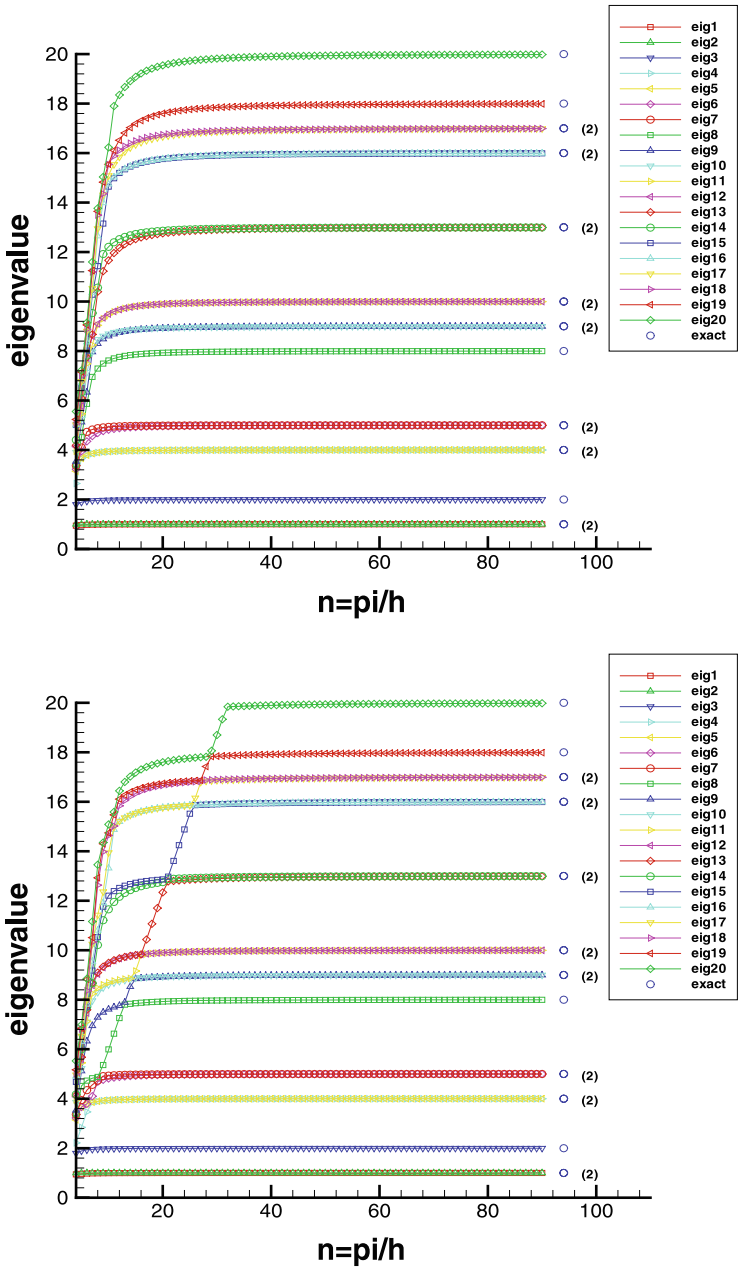

Fig. 8 First 20 Maxwell eigenvalues on $(0,\pi)^2$ computed by Eigensolver 2 (*top*) and its variant where the weight for the divergence term in (2.7) is h^{-1} (*bottom*), using conforming uniform meshes

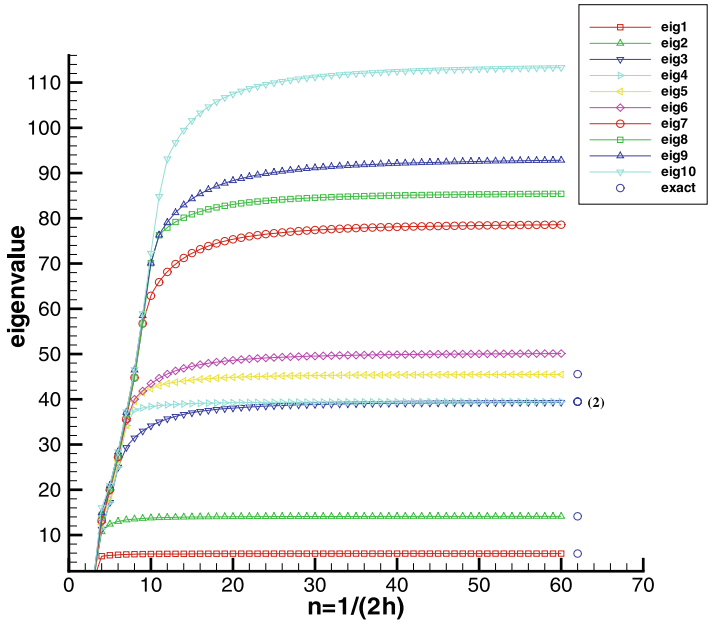

Fig. 9 First 10 Maxwell eigenvalues for the L-shaped domain computed by Eigensolver 2 using graded meshes

Table 3 First 5 Maxwell eigenvalues on $(0,\pi)^2$ computed by Eigensolver 2 using conforming uniform meshes

$n=\frac{\pi}{h}$	1st	Order	2nd	Order	3rd	Order	4th	Order	5th	Order
4	0.943	–	1.000	–	1.798	–	2.647	–	3.145	–
8	0.988	2.19	1.000	−0.40	1.967	2.60	3.895	3.69	3.896	3.04
16	0.997	2.07	1.000	1.26	1.993	2.27	3.977	2.21	3.977	2.20
32	0.999	2.03	1.000	1.72	1.998	2.12	3.995	2.08	3.995	2.08
64	1.000	2.01	1.000	1.87	2.000	2.05	3.999	2.03	3.999	2.03
128	1.000	2.01	1.000	1.94	2.000	2.03	4.000	2.01	4.000	2.01
Exact	1		1		2		4		4	

Table 4 First 5 Maxwell eigenvalues for the L-shaped domain computed by Eigensolver 2 using graded meshes

$n=\frac{1}{2h}$	1st	Order	2nd	Order	3rd	Order	4th	Order	5th	Order
4	5.319	–	10.726	–	11.275	–	11.440	–	12.349	–
8	5.756	1.99	13.532	2.50	31.448	1.81	37.651	3.94	39.529	2.46
16	5.867	2.05	13.992	2.07	37.307	1.89	39.100	2.27	44.429	2.42
32	5.894	2.08	14.101	2.03	38.929	1.98	39.390	2.10	45.291	2.08
64	5.901	2.08	14.127	2.01	39.341	2.00	39.457	2.05	45.493	2.03
Exact	5.902		14.136		39.478		39.478		45.558	

4.2.2 The Weight for the Divergence Term in (2.7)

The divergence-free constraint on eigenfunctions is imposed in Eigensolver 2 through the weight h^{-2} for the divergence term in (2.7). Here we explore the variant where the weight is h^{-1} by comparing in Fig. 8 the first 20 Maxwell eigenvalues for the square $(0, \pi)^2$ computed by the two schemes using conforming uniform meshes. Based on these plots, the following comments can be made.

1. The lower ranges of the numerical spectra computed by Eigensolver 2 and the variant are almost identical.
2. Eigensolver 2 can resolve the eigenvalues of different magnitudes very well even on relatively coarse meshes. For larger eigenvalues, the same level of resolution can only be achieved by the variant on finer meshes. This is confirmed further by the numerical results for the next 20 Maxwell eigenvalues (which are not reported).

We can understand these observations by considering the following eigenproblem: Find $(\boldsymbol{u}, \lambda) \in H_0(\mathrm{curl}; \Omega) \cap H(\mathrm{div}; \Omega)$ such that

$$(\nabla \times \boldsymbol{u}, \nabla \times \boldsymbol{v}) + \gamma(\nabla \cdot \boldsymbol{u}, \nabla \cdot \boldsymbol{v}) = \lambda(\boldsymbol{u}, \boldsymbol{v}), \tag{4.2}$$

for all $H_0(\mathrm{curl}; \Omega) \cap H(\mathrm{div}; \Omega)$. It follows from the results in [7] that this eigenproblem can be solved with second order accuracy using the finite element space W_h by replacing the weight h^{-2} in $b_{h,0}(\cdot, \cdot)$ with γ.

It is known [18] that the eigenvalues defined by (4.2) has the structure of $E_M \cup \gamma E_L$, where E_M is the set of Maxwell eigenvalues and E_L is the set of Laplace eigenvalues with homogeneous Dirichlet boundary condition. Therefore, for $\gamma = h^{-2}$ (Eigensolver 2) or $\gamma = h^{-1}$ (variant eigensolver), the lower ranges of the spectra defined by (1.1) and (4.2) become identical as $h \downarrow 0$ (i.e., $\gamma \uparrow \infty$), and the Maxwell eigenvalues can be captured by either scheme with second order accuracy.

4.2.3 Results for the Doubly Connected Domain

As discussed in Remark 2.2, unlike V_h, the discrete space W_h has a complete set of local bases for general domains, therefore Eigensolver 2 can be easily implemented for both simply and multiply connected domains. In this subsection, we consider the doubly connected domain $(0, 4)^2 \backslash (1, 3)^2$, where the meshes are graded around the re-entrant corners with grading parameter $\frac{1}{3}$ (Fig. 3, right).

Numerical results for the first 5 Maxwell eigenvalues computed by Eigensolver 2 are reported in Table 5, from which we can see that the scheme captures the zero Maxwell eigenvalue with the correct multiplicity one.

Note that for this example, Maxwell eigensolvers based on (1.2), such as the standard (symmetric, nonsymmetric or incomplete) interior penalty methods discussed in [12, 13], will produce numerical eigenvalues approximating the true Maxwell eigenvalue 0 with multiplicity one, as well as the non-physical zero eigenvalues whose eigenspace is infinite dimensional. Additional steps may be needed to separate these approximations for some applications, see [26].

4.3 Numerical Results for Eigensolver 3

In this subsection we present numerical results for Eigensolver 3. We will focus on the accuracy of the scheme, the role played by the last two terms in the definition of $c_{h,0}(\cdot, \cdot)$,

Table 5 First 5 Maxwell eigenvalues on the doubly connected domain $(0,4)^2 \setminus (1,3)^2$ computed by Eigensolver 2 using graded meshes

$n = \frac{1}{h}$	1st	2nd	3rd	4th	5th
2	0.716	0.925	0.925	1.301	2.896
4	0.396	0.661	0.661	1.146	2.200
8	0.175	0.471	0.471	1.080	1.784
16	0.063	0.373	0.373	1.054	1.586
32	0.020	0.335	0.335	1.045	1.511
64	0.006	0.322	0.322	1.042	1.486

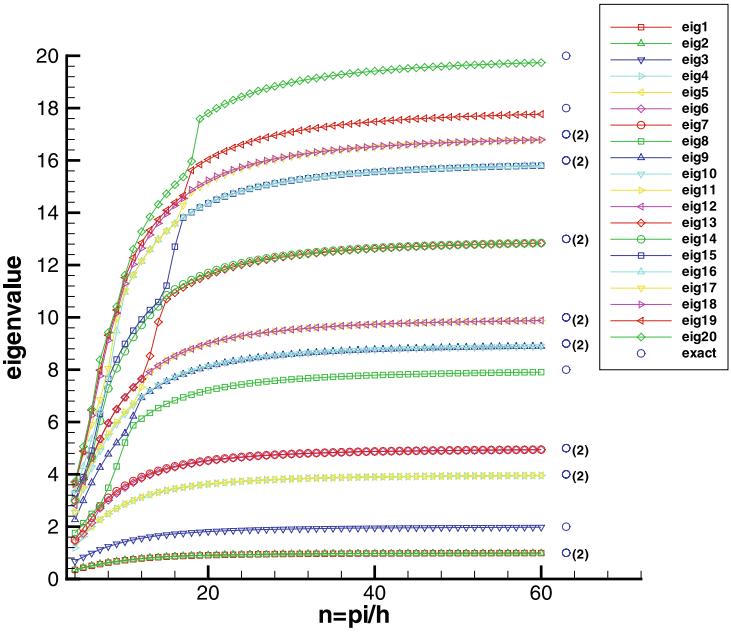

Fig. 10 First 20 Maxwell eigenvalues on $(0,\pi)^2$ computed by Eigensolver 3 using conforming uniform meshes

and the performance of the scheme on nonconforming meshes. Results similar to those reported in Sect. 4.1.2 for Eigensolver 1 and those in Sect. 4.2.3 for Eigensolver 2 also hold for Eigensolver 3 and will not be repeated here.

4.3.1 Accuracy of the Scheme

In the first experiment we compute the Maxwell eigenvalues for the square $(0,\pi)^2$ using conforming uniform meshes. Figure 10 contains the plot of the first 20 numerical eigenvalues versus the parameter $n = \pi/h$, which shows that the eigenvalues are well resolved and there is no spurious eigenmode. The performance of this solver is not quite as good as Eigensolver 1 and Eigensolver 2 for meshes that are relatively coarse. We can also see from Table 6 that the numerical approximations converge with second order accuracy, which confirms our error estimate (3.8).

Table 6 First 5 Maxwell eigenvalues on $(0,\pi)^2$ computed by Eigensolver 3 using conforming uniform meshes

$n=\frac{\pi}{h}$	1st	Order	2nd	Order	3rd	Order	4th	Order	5th	Order
4	0.347	–	0.367	–	0.673	–	1.188	–	1.409	–
8	0.626	0.80	0.634	0.79	1.239	0.80	2.495	0.90	2.496	0.78
16	0.863	1.45	0.866	1.45	1.723	1.46	3.446	1.44	3.446	1.44
32	0.962	1.84	0.963	1.84	1.923	1.84	3.845	1.83	3.845	1.83
64	0.990	1.97	0.990	1.97	1.980	1.97	3.960	1.96	3.960	1.96
128	0.998	1.97	0.998	2.00	1.995	2.01	3.990	1.99	3.990	1.99
Exact	1		1		2		4		4	

Table 7 First 5 Maxwell eigenvalues for the L-shaped domain $(-0.5,0.5)^2 \setminus [0,0.5]^2$ computed by Eigensolver 3 using graded meshes

$n=\frac{1}{2h}$	1st	Order	2nd	Order	3rd	Order	4th	Order	5th	Order
4	4.747	–	9.963	–	11.233	–	11.316	–	12.226	–
8	5.574	1.81	13.102	2.01	30.631	1.67	36.653	3.32	38.548	2.25
16	5.819	1.98	13.875	1.98	37.008	1.84	38.822	2.11	44.091	2.26
32	5.882	2.02	14.071	2.00	38.847	1.97	39.319	2.04	45.204	2.05
64	5.897	1.97	14.120	2.02	39.320	2.00	39.439	2.03	45.471	2.02
Exact	5.902		14.136		39.478		39.478		45.558	

In the second experiment we compute the Maxwell eigenvalues for the L-shaped domain using graded meshes. Table 7 contains the first 5 numerical eigenvalues which shows that the scheme has second order accuracy. Results for the first 10 Maxwell eigenvalues are plotted in Fig. 11, from which one can see that there is no spurious eigenmode.

4.3.2 The Role of the Last Two Terms in (2.9)

The last two penalization terms in the bilinear form $c_{h,0}(\cdot,\cdot)$ are included to compensate for the lack of any continuity for the vector fields in the space U_h. Numerical examples in [9] indicate that without these two terms the numerical scheme for the source problem (1.3) will fail to converge. In this subsection we examine the numerical spectrum of the variant of Eigensolver 3 where the last two penalization terms in (2.9) are absent.

The first 40 eigenvalues for the square $(0,\pi)^2$ computed by the variant eigensolver using conforming uniform meshes are presented in Fig. 12. One can see that there are many spurious eigenvalues, which again confirms the necessity of these two penalization terms.

4.3.3 Results with Nonconforming Meshes

As discussed in Remark 3.4, the error estimates in Theorem 3.1 hold for Eigensolver 3 when it is applied to both conforming and n-irregular nonconforming meshes. In this subsection we show the performance of Eigensolver 3 when it is applied to the square $(0,\pi)^2$ with the 1-irregular nonconforming mesh depicted in Fig. 1 (right), where the domain is first divided into $\Omega_1=(0,\frac{\pi}{2})\times(0,\pi)$ and $\Omega_2=(\frac{\pi}{2},\pi)\times(0,\pi)$, and then conforming meshes

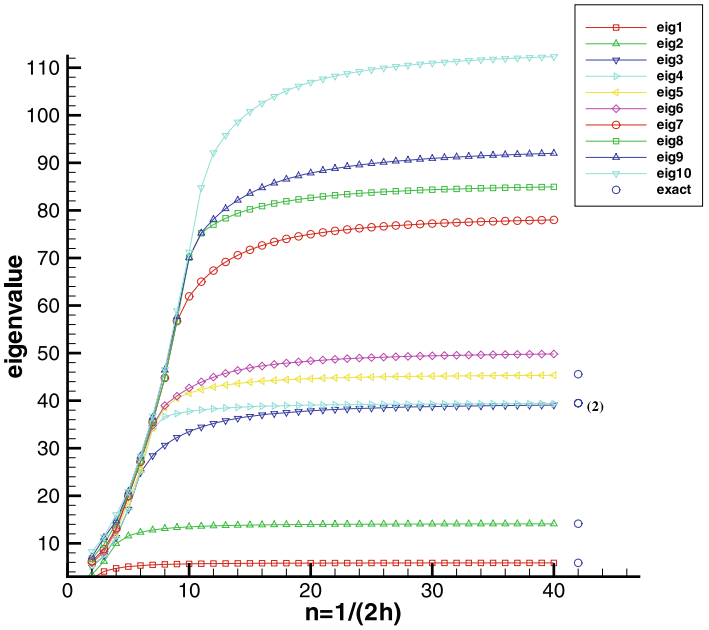

Fig. 11 First 10 Maxwell eigenvalues for the L-shaped domain computed by Eigensolver 3 using graded meshes

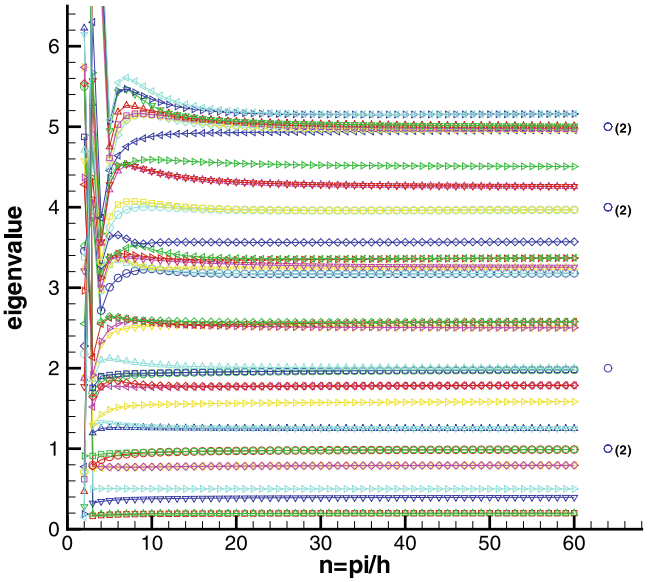

Fig. 12 First 40 numerical eigenvalues on $(0,\pi)^2$ computed by the variant of Eigensolver 3 where the last two terms in (2.9) are absent

Table 8 First 5 Maxwell eigenvalues on $(0,\pi)^2$ computed by Eigensolver 3 using nonconforming meshes

$n=\frac{\pi}{h}$	1st	Order	2nd	Order	3rd	Order	4th	Order	5th	Order
4	0.331	–	0.349	–	0.652	–	1.077	–	1.307	–
8	0.603	0.75	0.611	0.74	1.200	0.75	2.389	0.86	2.433	0.78
16	0.851	1.41	0.853	1.40	1.699	1.41	3.392	1.41	3.404	1.39
32	0.958	1.82	0.958	1.81	1.915	1.82	3.828	1.82	3.830	1.81
64	0.990	1.96	0.989	1.96	1.978	1.96	3.956	1.96	3.956	1.96
128	0.997	1.99	0.997	1.99	1.995	1.99	3.989	1.99	3.989	1.99
Exact	1		1		2		4		4	

are introduced on Ω_1 and Ω_2 separately, with the hanging nodes uniformly spaced along a given edge on $\Gamma=\partial\Omega_1\cap\partial\Omega_2$. For such meshes, we define $\mathcal{E}_h$ by

$$\mathcal{E}_h=\{e\in\partial T : T\in\mathcal{T}_h \text{ and } T\subset\Omega_1\}\cup\{e\in\partial T\backslash\Gamma : T\in\mathcal{T}_h \text{ and } T\subset\Omega_2\}.$$

The subset of $\mathcal{E}_h$ interior to Ω is denoted by $\mathcal{E}_h^i$.

Table 8 contains the first 5 Maxwell eigenvalues computed by Eigensolver 3 using such nonconforming meshes. It shows that Eigensolver 3 remains second order accurate and it generates no spurious eigenvalues, and its performance is comparable with the performance on conforming meshes (Table 6).

5 Detection of Spurious Eigenmodes

In this section we discuss numerical techniques that can detect the spurious eigenmodes generated by the T-type and N-type variants of Eigensolver 1 introduced in Sect. 4.1.2 and turn these variants into effective Maxwell eigensolvers. These techniques may also contribute to the development of methods that can detect spurious eigenmodes generated by other Maxwell eigensolvers (cf. for example [5, 23]).

Given $\boldsymbol{w}\in V_h$, we define

$$|\boldsymbol{w}|_{t,h}=\left\{\sum_{e\in\mathcal{E}_h}\frac{[\Phi_\mu(e)]^2}{|e|}\int_e[\![\boldsymbol{w}]\!]_t^2\,ds\right\}^{1/2}, \tag{5.1}$$

$$|\boldsymbol{w}|_{\mathrm{div},h}=\left\{\sum_{e\in\mathcal{E}_h^i}\frac{[\Phi_\mu(e)]^2}{|e|}\int_e[\![\boldsymbol{w}]\!]_n^2\,ds\right\}^{1/2}. \tag{5.2}$$

Note that $|\boldsymbol{w}|_{t,h}$ measures the conformity of $\boldsymbol{w}$ with respect to the space $H_0(\mathrm{curl};\Omega)$, while $|\boldsymbol{w}|_{\mathrm{div},h}$ measures the conformity of $\boldsymbol{w}$ with respect to the space $H(\mathrm{div};\Omega)$ (and hence the space $H(\mathrm{div}^0;\Omega)$, since vector fields in V_h are locally divergence-free).

Since the Maxwell eigenfunctions defined by (1.1) belong to $H_0(\mathrm{curl};\Omega)\cap H(\mathrm{div}^0;\Omega)$, in order for a sequence of discrete eigenfunctions $\{\boldsymbol{v}_h\}_h$ with $\boldsymbol{v}_h\in V_h$ to approximate an eigenfunction, the following conditions are necessary:

$$\lim_{h\to0}|\boldsymbol{v}_h|_{t,h}=0, \tag{5.3}$$

$$\lim_{h\to 0} |\boldsymbol{v}_h|_{\mathrm{div},h} = 0. \tag{5.4}$$

This is confirmed by examining the log-log plot of $|\mathring{\boldsymbol{u}}_h|_{\mathrm{div},h}$ (resp. $|\mathring{\boldsymbol{u}}|_{t,h}$) versus $n = \pi/h$ on the left (resp. right) side of the top row of Fig. 13, where $\mathring{\boldsymbol{u}}_h$ is the discrete eigenfunction for the square $(0,\pi)^2$ computed by Eigensolver 1 and normalized so that $\|\mathring{\boldsymbol{u}}_h\|_{L_2(\Omega)} = 1$. We can see that both $|\mathring{\boldsymbol{u}}_h|_{\mathrm{div},h}$ and $|\mathring{\boldsymbol{u}}_h|_{t,h}$ for the discrete eigenfunctions corresponding to the first 20 discrete eigenvalues decay steadily to 0, mirroring the fact that the discrete eigenfunctions computed by Eigensolver 1 converge to the Maxwell eigenfunctions (Theorem 3.1).

We have also computed the first 20 eigenvalues for the square $(0,\pi)^2$ by the T-type variant of Eigensolver 1 defined by (4.1) with $C_{p,n} = 0$ and $C_{p,t} = 30$. On the bottom row of Fig. 13, we present the log-log plots of $|\mathring{\boldsymbol{u}}_h|_{\mathrm{div},h}$ (left) and $|\mathring{\boldsymbol{u}}_h|_{t,n}$ (right) versus $n = \pi/h$, where the $\mathring{\boldsymbol{u}}_h$'s are the normalized discrete eigenfunction. We can see that (5.3) and (5.4) hold for some but not all discrete eigenfunctions, which agree with the plot in the middle row on the left of Fig. 6 and demonstrate the existence of spurious eigenmodes for the T-type variant.

To better understand the behavior of these numerical eigenfunctions, we present the data in a different way in Fig. 14, where bright colors indicate the violation of (5.4) (left) or (5.3) (right). Based on Figs. 13 and 14, we can assert, for example, that (i) when $n = 50$, the 11th, 14th, 19th numerical eigenvalues are spurious, (ii) when $n = 70$, the 11th, 14th and 17th numerical eigenvalues are spurious, and (iii) when $n = 85$, the 9th, 14th and 15th numerical eigenvalues are spurious. These assertions agree with the results in Fig. 6. Under a more careful examination of the numerical results, one can conclude that (5.3) and (5.4) are necessary and sufficient for the numerical eigenvalues computed by the T-type variant of Eigensolver 1 to approximate physical Maxwell eigenvalues.

We have also performed a similar numerical study for the L-shape domain, computing the first 10 discrete eigenvalues by the TN-type, T-type and N-type variants using graded meshes. The plots in Figs. 15 and 16 confirm that both the TN-type and T-type variants produce accurate approximations for the Maxwell eigenvalues. The same holds for the N-type variant, except for the 3 spurious zero eigenvalues. These results are consistent with the plots in Fig. 7.

Similar tests can also be performed for the variants of Eigensolver 2 and Eigensolver 3, as long as the definitions of (5.1) and (5.2) are modified accordingly. For instance, to detect spurious eigenmodes for the variants of Eigensolver 2, one needs to modify the definition of (5.2) to include the numerical divergence contributed by $\sum_{T\in\mathcal{T}_h} \|\nabla_h \cdot \boldsymbol{w}\|^2_{L_2(T)}$.

6 Concluding Remarks

Our previous work [8–10] on the source problem for the time-harmonic Maxwell equations indicates that the Maxwell eigenproblem (1.1) can also be solved by nonconforming finite element methods. However, only Eigensolver 3 has been analyzed in [9]. In this paper we have presented a unified analysis and performed thorough numerical tests for all three nonconforming Maxwell eigensolvers.

Our results show that these Maxwell eigensolvers have optimal order convergence on properly graded meshes and they do not generate any spurious eigenmodes even on relatively coarse meshes. Furthermore, they impose just the right amount of continuity across element interfaces without having to choose any parameters.

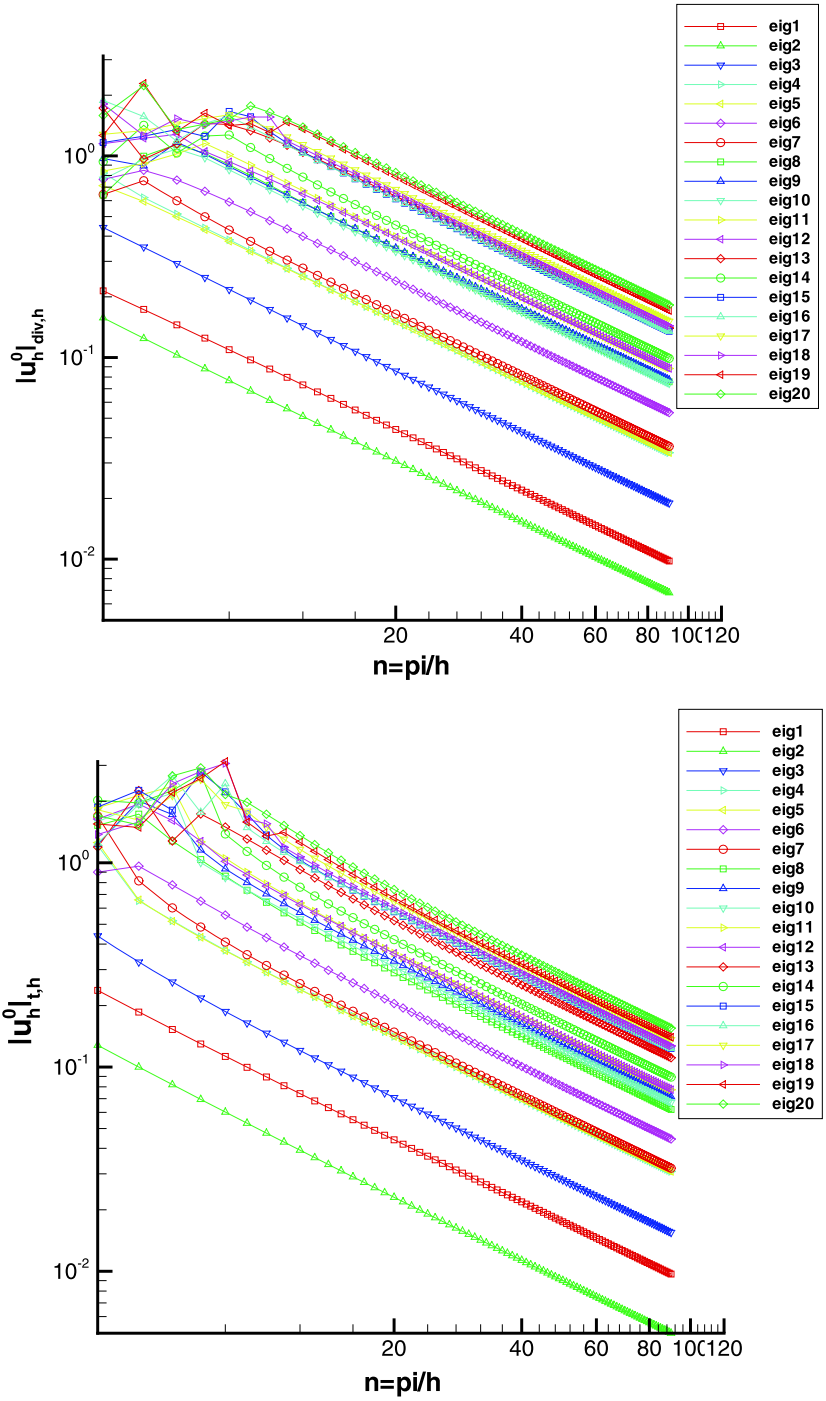

Fig. 13 Log-log plots of $|\mathring{u}_h|_{\mathrm{div},h}$ (*left*) and $|\mathring{u}_h|_{t,n}$ (*right*) versus n, where $n = \pi/h$, for the TN-type eigensolver (*top*, with $C_{p,n} = C_{p,t} = 1$ in (4.1)) and the T-type eigensolver (*bottom*, with $C_{p,n} = 0$ and $C_{p,t} = 30$ in (4.1)) on $(0, \pi)^2$ with conforming uniform meshes

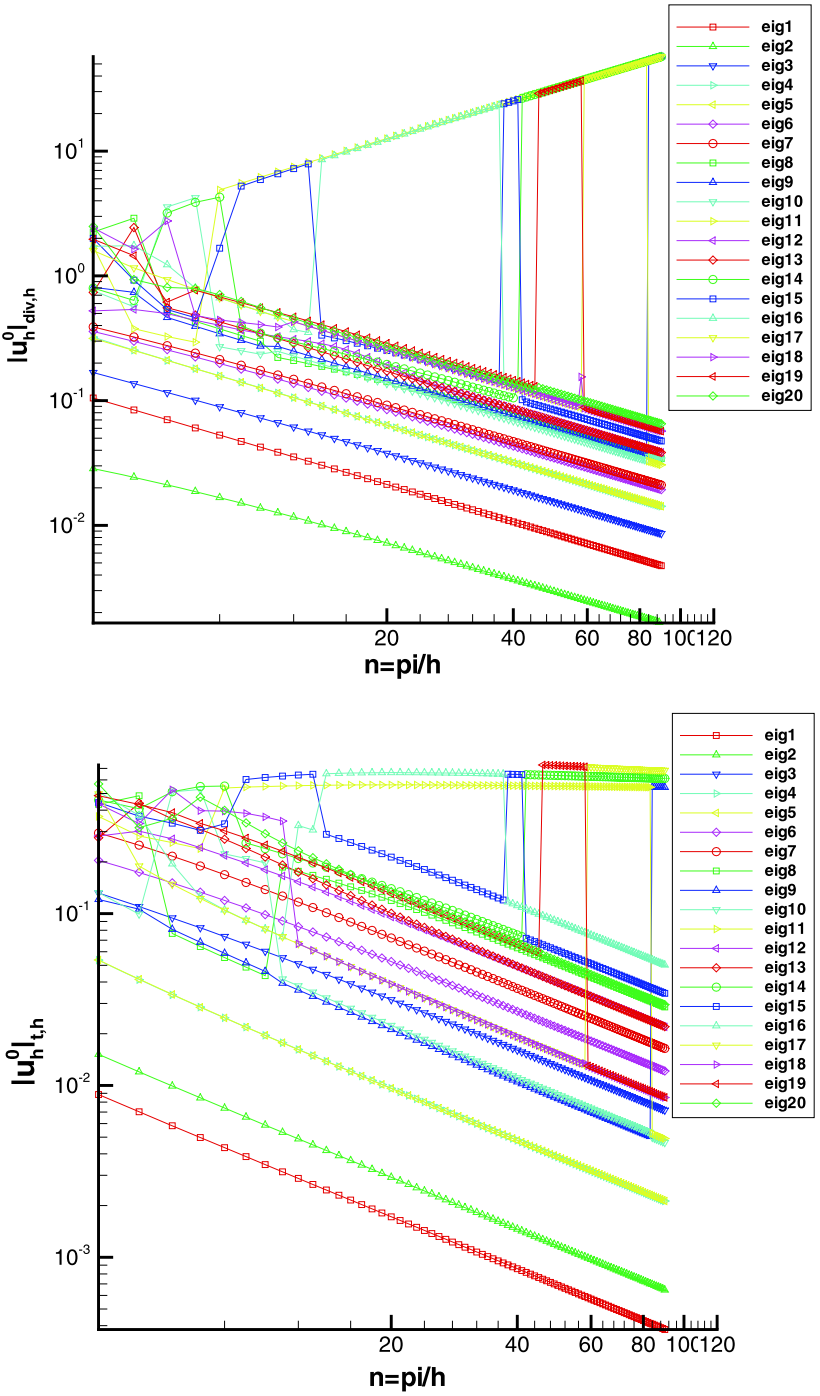

Fig. 13 (*Continued*)

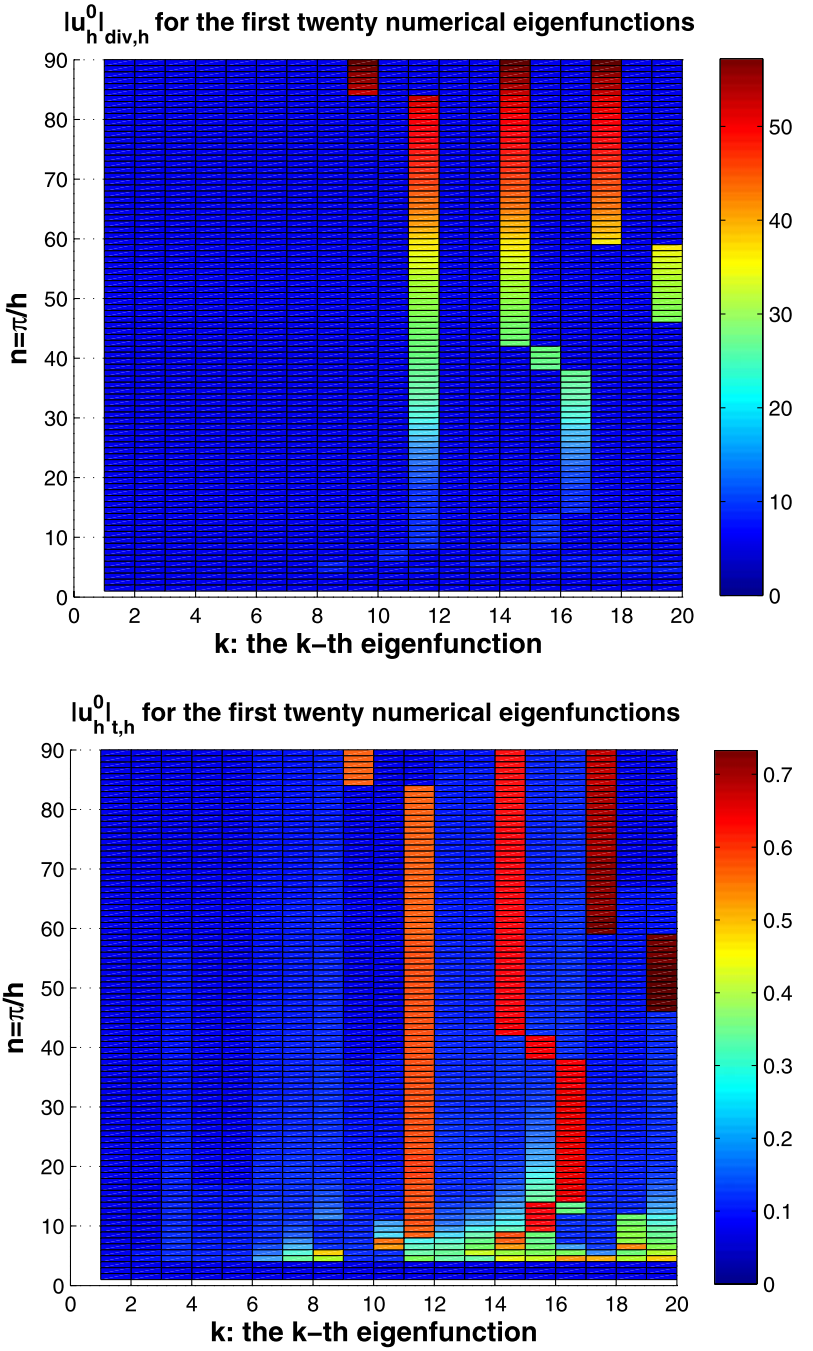

Fig. 14 $|\mathring{\boldsymbol{u}}_h|_{\mathrm{div},h}$ (*left*) and $|\mathring{\boldsymbol{u}}_h|_{t,h}$ (*right*) versus different $n = \pi/h$, for normalized discrete eigenfunctions corresponding to the first 20 numerical eigenvalues computed by the T-type variant of Eigensolver 1 (with $C_{p,n} = 0$ and $C_{p,t} = 30$ in (4.1)) on $(0, \pi)^2$ using conforming uniform meshes

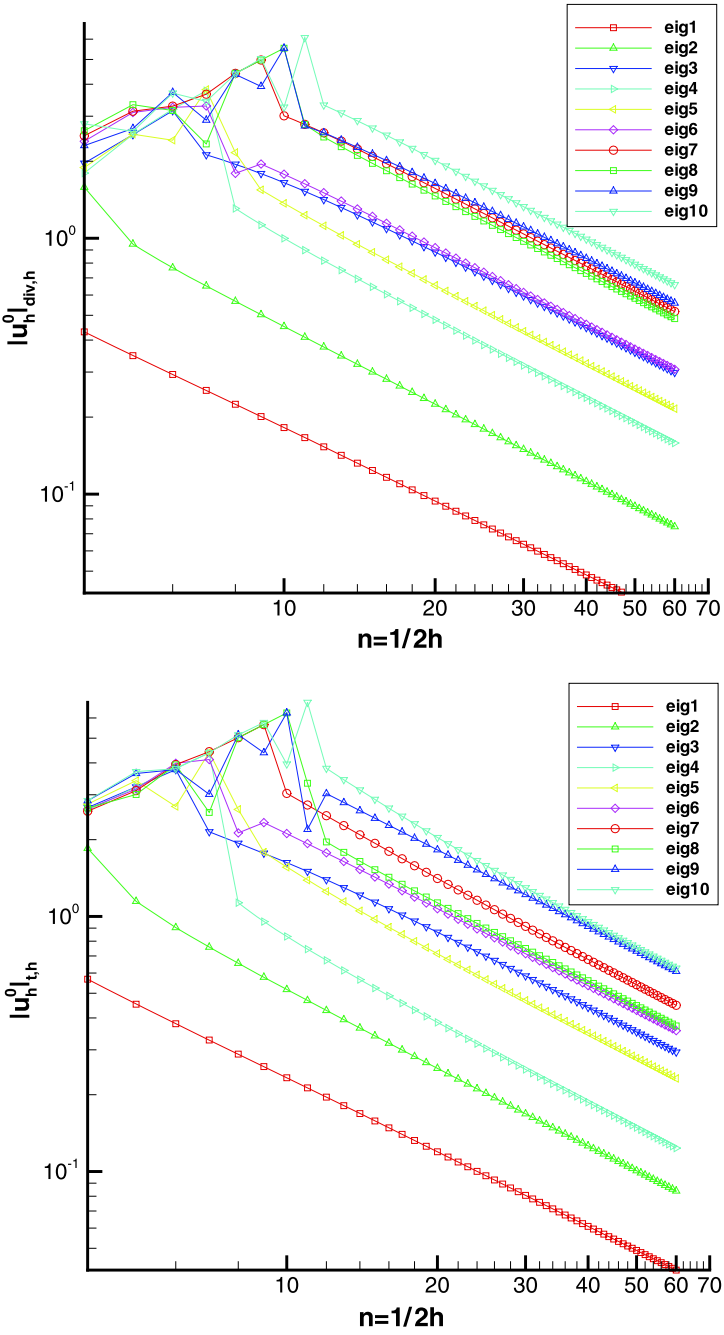

Fig. 15 Log-log plots of $|\mathring{\boldsymbol{u}}_h|_{\mathrm{div},h}$ (*left*) and $|\mathring{\boldsymbol{u}}_h|_{t,n}$ (*right*) versus n, where $n = 1/(2h)$, for the TN-type eigensolver (*top*, with $C_{p,n} = C_{p,t} = 1$ in (4.1)) the T-type eigensolver (*middle*, with $C_{p,n} = 0$ and $C_{p,t} = 25$ in (4.1)) and the N-type eigensolver (*bottom*, with $C_{p,n} = 25$ and $C_{p,t} = 0$ in (4.1)) on the L-shape domain with graded meshes

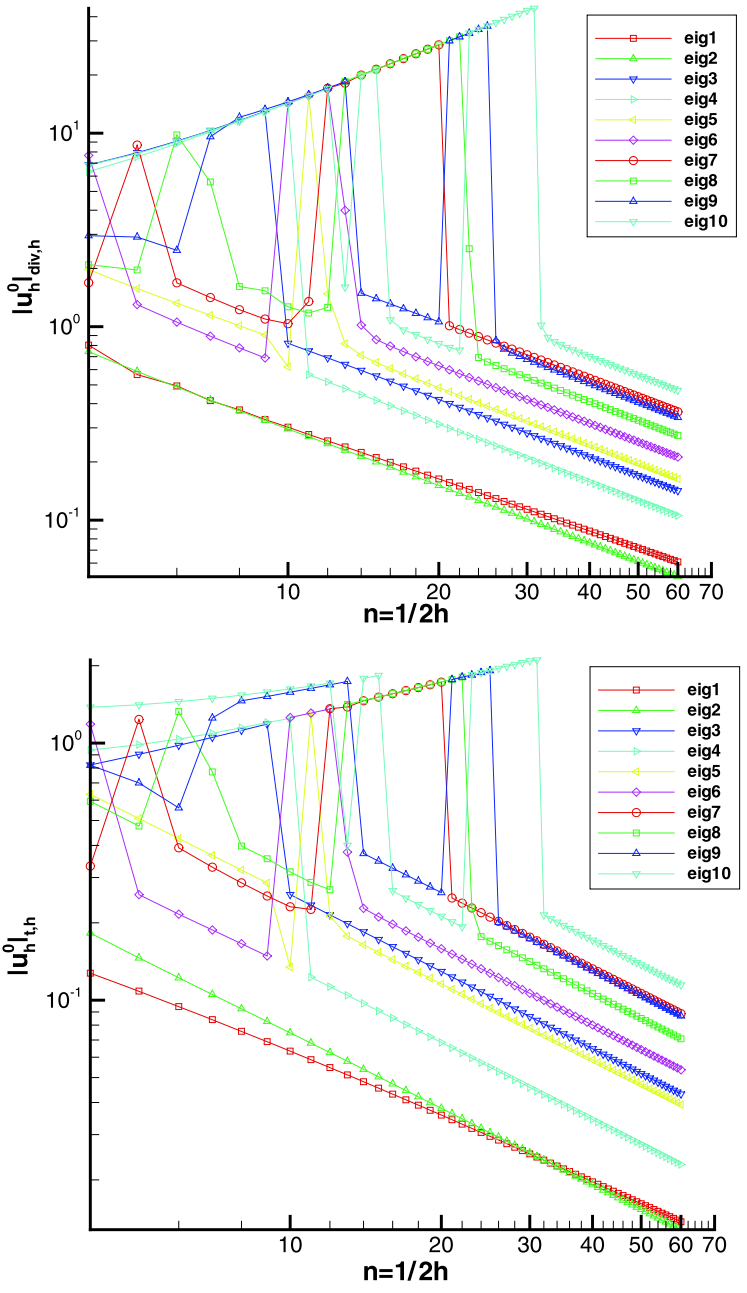

Fig. 15 (*Continued*)

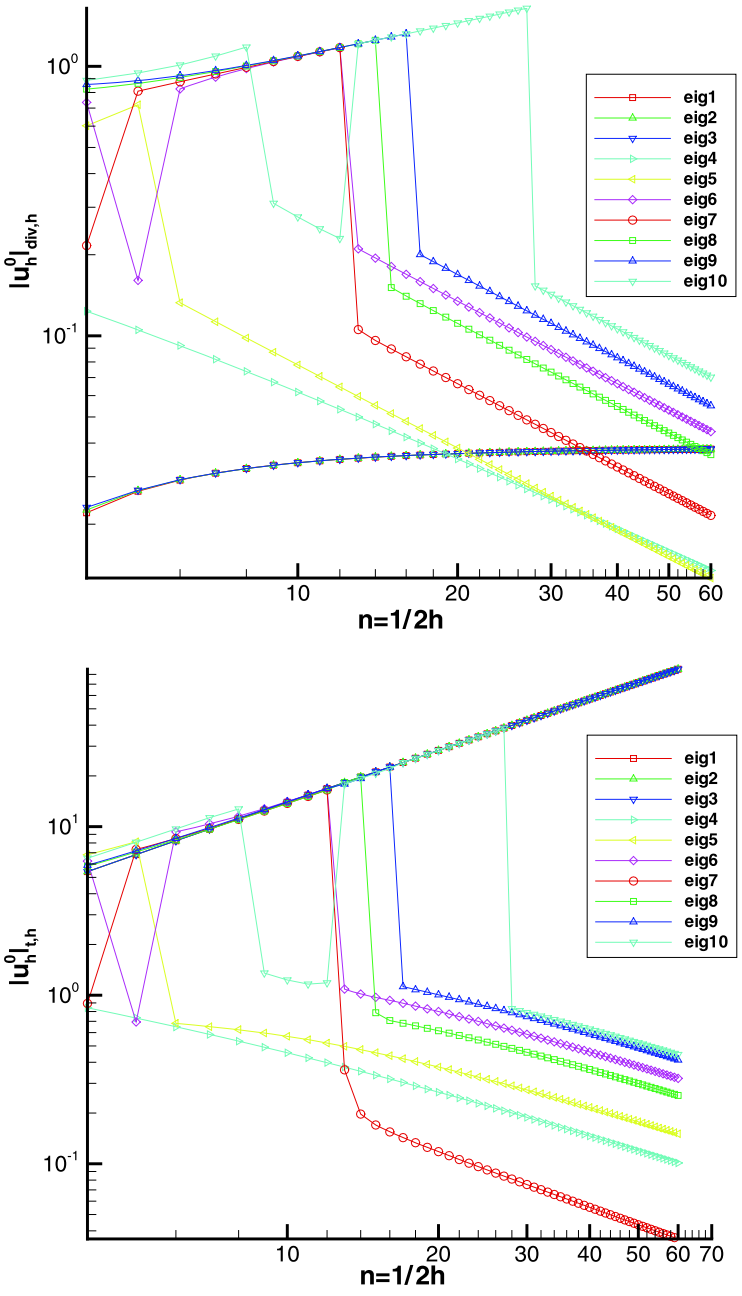

Fig. 15 (*Continued*)

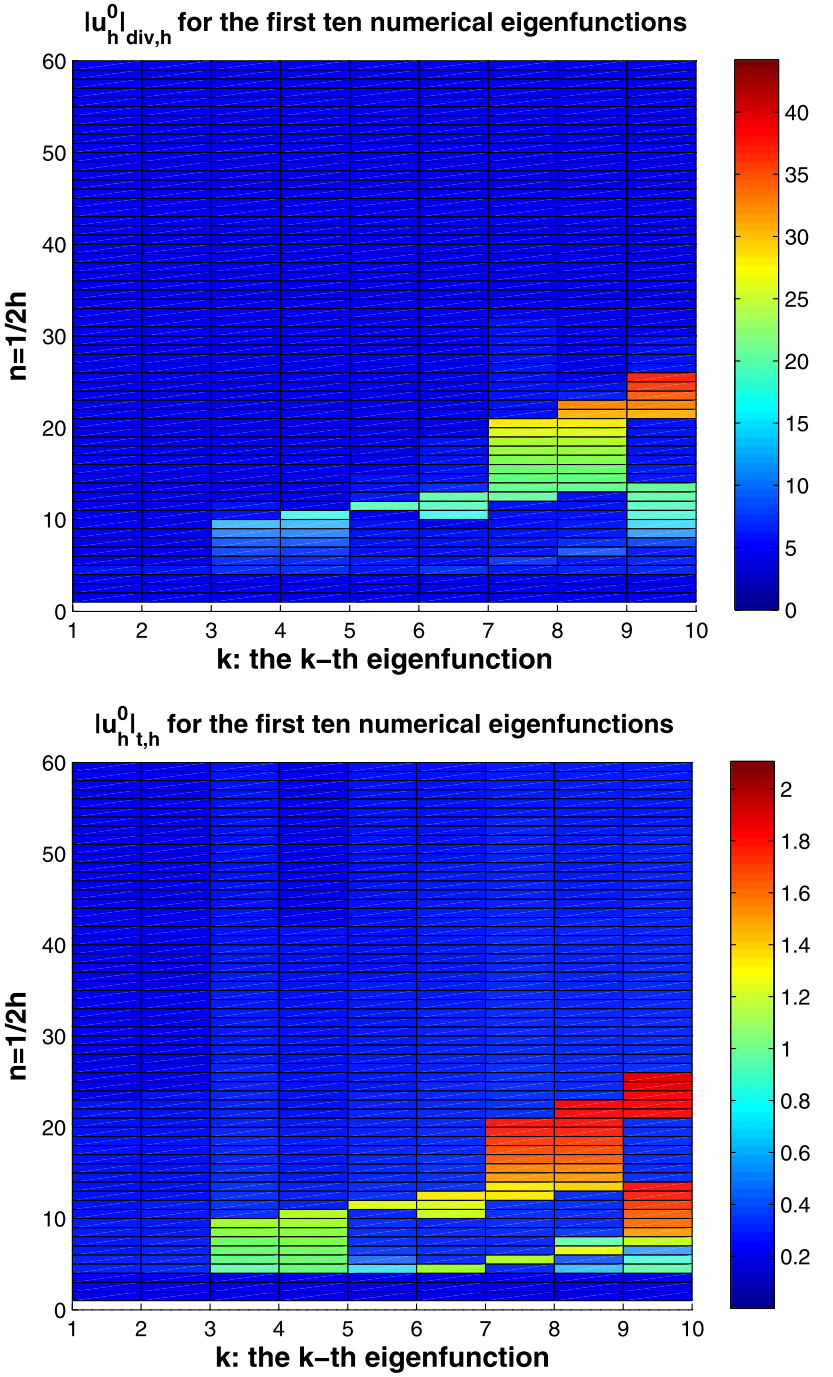

Fig. 16 $|\mathring{\boldsymbol{u}}_h|_{\mathrm{div},h}$ (*left*) and $|\mathring{\boldsymbol{u}}_h|_{t,h}$ (*right*) versus different $n = 1/(2h)$, for normalized discrete eigenfunctions corresponding to the first 10 numerical eigenvalues computed by the T-type variant of Eigensolver 1 (*top*, with $C_{p,n} = 0$ and $C_{p,t} = 25$ in (4.1)) and the N-type variant of Eigensolver 1 (*bottom*, with $C_{p,n} = 25$ and $C_{p,t} = 0$ in (4.1)) for the L-shaped domain using graded meshes

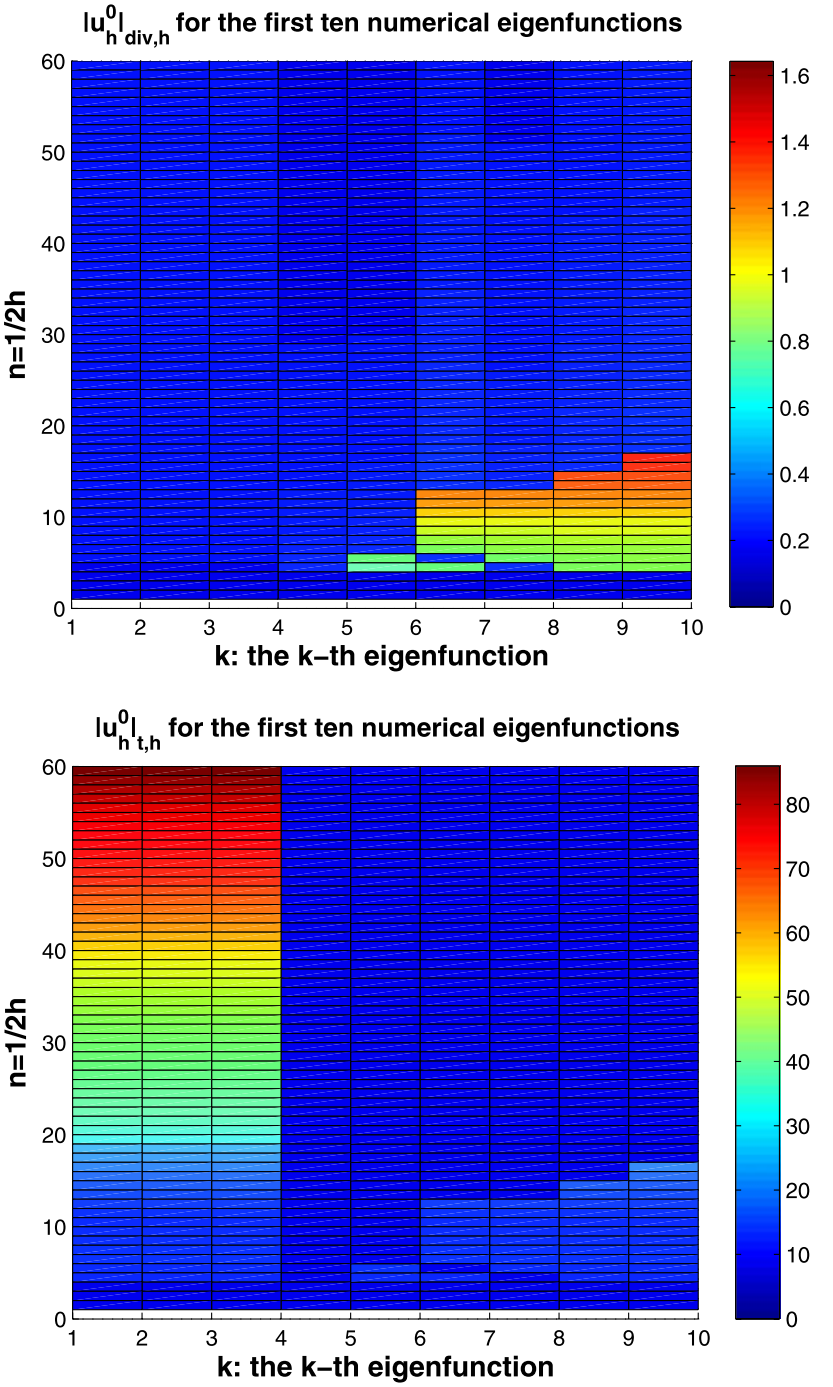

Fig. 16 (*Continued*)

We have demonstrated the capability of these eigensolvers for multiply connected domains and nonconforming meshes. We have also developed numerical techniques that can detect the spurious eigenmodes generated by some variants of these eigensolvers.

Our schemes can be extended to the higher order vector finite elements proposed in [11]. The extension to three dimensional electromagnetic problems as well as the development of fast solvers for these schemes are subjects of our ongoing research.

Acknowledgement The authors would like to thank Guido Kanschat for helpful discussions concerning the material in Sect. 5.

References

1. Arnold, D.N.: An interior penalty finite element method with discontinuous elements. SIAM J. Numer. Anal. **19**, 742–760 (1982)
2. Assous, F., Ciarlet, P. Jr., Sonnendrücker, E.: Resolution of the Maxwell equation in a domain with reentrant corners. Math. Model. Numer. Anal. **32**, 359–389 (1998)
3. Babuška, I., Osborn, J.: Eigenvalue Problems. In: Ciarlet, P.G., Lions, J.L. (eds.) Handbook of Numerical Analysis II, pp. 641–787. North-Holland, Amsterdam (1991)
4. Boffi, D.: Fortin operators and discrete compactness for edge elements. Numer. Math. **87**, 229–246 (2000)
5. Boffi, D., Fernandes, P., Gastaldi, L., Perugia, I.: Computational models of electromagnetic resonators: analysis of edge element approximation. SIAM J. Numer. Anal. **36**, 1264–1290 (1999)
6. Boffi, D., Kikuchi, F., Schöberl, J.: Edge element computation of Maxwell's eigenvalues on general quadrilateral meshes. Math. Models Methods Appl. Sci. **16**, 265–273 (2006)
7. Brenner, S.C., Cui, J., Li, F., Sung, L.-Y.: A nonconforming finite element method for a two-dimensional curl-curl and grad-div problem. Numer. Math. **109**, 509–533 (2008)
8. Brenner, S.C., Li, F., Sung, L.-Y.: A locally divergence-free nonconforming finite element method for the reduced time-harmonic Maxwell equations. Math. Comput. **76**, 573–595 (2007)
9. Brenner, S.C., Li, F., Sung, L.-Y.: A locally divergence-free interior penalty method for two-dimensional curl-curl problems. SIAM J. Numer. Anal. **46**, 1190–1211 (2008)
10. Brenner, S.C., Li, F., Sung, L.-Y.: A nonconforming penalty method for two dimensional curl-curl problems. Math. Models Methods Appl. Sci. (to appear)
11. Brenner, S.C., Sung, L.-Y.: A quadratic nonconforming vector finite element for $H(\mathrm{curl};\Omega)\cap H(\mathrm{div};\Omega)$. Appl. Math. Lett. doi:10.1016/j.aml.2008.07.017
12. Buffa, A., Houston, P., Perugia, I.: Discontinuous Galerkin computation of the Maxwell eigenvalues on simplical meshes. J. Comput. Appl. Math. **204**, 317–333 (2007)
13. Buffa, A., Perugia, I.: Discontinuous Galerkin approximation of the Maxwell eigenproblem. SIAM J. Numer. Anal. **44**, 2198–2226 (2006)
14. Caorsi, S., Fernandes, P., Raffetto, M.: On the convergence of Galerkin finite element approximations of electromagnetic eigenproblems. SIAM J. Numer. Anal. **38**, 580–607 (2000)
15. Caorsi, S., Fernandes, P., Raffetto, M.: Spurious-free approximations of electromagnetic eigenproblems by means of Nédélec-type elements. Math. Model. Numer. Anal. **35**, 331–358 (2001)
16. Chatelin, F.: Spectral Approximations of Linear Operators. Academic Press, San Diego (1983)
17. Costabel, M.: A remark on the regularity of solutions of Maxwell's equations on Lipschitz domains. Math. Methods Appl. Sci. **12**, 365–368 (1990)
18. Costabel, M., Dauge, M.: Maxwell and Lamé eigenvalues on polyhedra. Math. Methods Appl. Sci. **22**, 243–258 (1999)
19. Costabel, M., Dauge, M.: Singularities of electromagnetic fields in polyhedral domains. Arch. Ration. Mech. Anal. **151**, 221–276 (2000)
20. Costabel, M., Dauge, M.: Weighted regularization of Maxwell equations in polyhedral domains. Numer. Math. **93**, 239–277 (2002)
21. Crouzeix, M., Raviart, P.-A.: Conforming and nonconforming finite element methods for solving the stationary Stokes equations I. RAIRO Anal. Numér. **7**, 33–75 (1973)
22. Dunford, N., Schwartz, J.T.: Linear Operators II. Wiley-Interscience, New York (1963)
23. Hesthaven, J.S., Warburton, T.: High order nodal discontinuous Galerkin methods for the Maxwell eigenvalue problem. Philos. Trans. R. Soc. Lond. Ser. A **362**, 493–524 (2004)
24. Kato, T.: Perturbation Theory of Linear Operators. Springer, Berlin (1966)

25. Monk, P.: Finite Element Methods for Maxwell's Equations. Numerical Mathematics and Scientific Computation. Oxford University Press, London (2003)
26. Levillain, V.: Eigenvalue approximation by a mixed method for resonant inhomogeneous cavities with metallic boundaries. Math. Comput. **58**, 11–20 (1992)
27. Warburton, T., Embree, M.: On the role of the penalty in the local discontinuous Galerkin method for Maxwell's eigenvalue problem. Comput. Mech. Appl. Eng. **195**, 3205–3223 (2006)